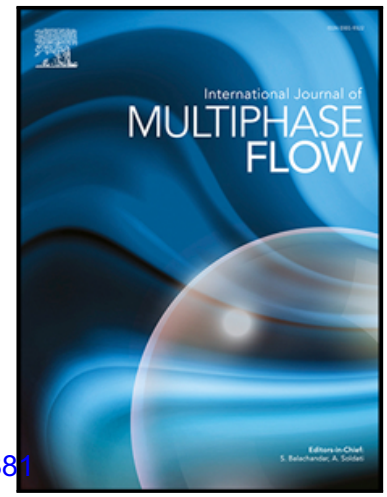

Development of a More Accurate Dynamic Bias Error Model for Two-Phase Flow Measurements Performed with Radiation Transmission

Julio Diaz , J.J. Serrano-Aguilera , Victor Petrov , Annalisa Manera

PII: S0301-9322(21)00296-2
DOI: https://doi.org/10.1016/j.ijmultiphaseflow.2021.103881
Reference: IJMF 103881

To appear in: *International Journal of Multiphase Flow*

Received date: 21 May 2021
Revised date: 17 September 2021
Accepted date: 25 October 2021

Please cite this article as: Julio Diaz , J.J. Serrano-Aguilera , Victor Petrov , Annalisa Manera , Development of a More Accurate Dynamic Bias Error Model for Two-Phase Flow Measurements Performed with Radiation Transmission, *International Journal of Multiphase Flow* (2021), doi: https://doi.org/10.1016/j.ijmultiphaseflow.2021.103881

Highlights

- A new dynamic bias model is formulated based on cyclical rectangular signals
- The new model incorporates the influence of the signal's temporal distribution
- Validation of the model is attained with simple signals and wire-mesh-sensor data
- The RMSE of the new model improves as much as ~60% compared to previous models

Development of a More Accurate Dynamic Bias Error Model for Two-Phase Flow Measurements Performed with Radiation Transmission

Julio Diaz[a], J.J. Serrano-Aguilera[b], Victor Petrov[a,c,d], Annalisa Manera[a,c,d]

[a]Department of Nuclear Engineering & Radiological Sciences, University of Michigan, 2355 Bonisteel Blvd., Ann Arbor, MI 48109, USA

[b]Universidad de Málaga, Escuela de Ingenierías Industriales, Campus de Teatinos s/n, Málaga, 29071, Spain

[c]ETH Zürich, Department of Mechanical and Process Engineering, Sonneggstrasse 3, 8092, Zürich, Switzerland

[d]Laboratory for Reactor Physics and Thermal-Hydraulics (LRT), Paul Scherrer Institut, 5232 Villigen PSI, Switzerland

juliod@umich.edu; jj.serragui@uma.es; petrov@umich.edu; manera@umich.edu.

ABSTRACT

Application of radiation transmission measurement of two-phase flow phenomena has surged in the past decades due to the advancements in radiation detection along with its non-intrusive nature in comparison with other advanced two-phase flow measurements instrumentation such as wire mesh sensors and needle probes. However, radiation transmission measurement entails various levels of complexity when measuring temporally varying signals, which is the case for two-phase flow phenomena. The time-integrated radiation transmission acquisition yields a biased result, known as dynamic bias. In the present study, a more accurate method to estimate the dynamic bias is formulated. In addition, the behavior of the dynamic bias in two-phase flow measurements is investigated and characterized as a function of the void-fraction's temporal phase distribution, the gas phase magnitude distribution, and the contrast attenuation between the liquid and gas phases. Both numerical simulations and actual measurements of two-phase flows obtained with wire-mesh sensors, which includes several flow patterns, are used in the study. The dynamic bias was simulated for a contrast attenuation factor, λ, ranging from 0.01 to 5; this is a dimensionless factor that considers the geometry, elemental composition of the phases, radiation type and energy. The RMSE error was estimated for the proposed model and the reference model derived by Harms; the RMSE percentage decrease for the proposed model relative to Harm's for the range of λ improves by 50% to 58% for the bubbly regime, 40% to 59% for the bubbly to churn transitional regime, 36% to 56% for the churn regime, and 15% to 56% for the wispy annular.

KEYWORDS

Radiation Transmission, Void Fraction, Dynamic Bias, Two-Phase Flow

NOMENCLATURE

Roman Variables

A	Component area
a	Lower integration limit
b	Upper integration limit
D	Total flow chord length
d	Chord length
f	Frequency
I	Radiation count-rate/flux
J	Superficial velocity
M	Number of recorded measurements
T	Signal period/Integration period
t	Time
u	Conductivity

Greek Variables

α	Void fraction
β	Sampling to phenomena period ratio
$\Delta\alpha$	Dynamic bias
δ	Pipe thickness
ε	Phase amplitude component
Θ	Centroid value
λ	Contrast attenuation factor
μ	Linear attenuation coefficient
ξ	Peak-to-peak amplitude
σ	Standard deviation
τ	Signal integration time
ω	Phase temporal-distribution/duty-cycle

Subscripts & Superscripts

2φ	Two-phase flow
$cent$	Centroid
CL	Center line
cr	Critical duty cycle
d	Detector subscript
G	Gas phase
i	Indexing variable
$ideal$	Reference
k	Indexing variable
L	Liquid phase
m	Discrete time variable
max	Maximum
$model$	Derived model
n	Discrete sampling variable
o	Source subscript
$Rect$	Rectangular signal

$Sine$	Sinusoidal signal
s	Sampled
Tri	Triangular signal
$+$	Active or positive portion
$-$	Passive or negative portion
$\sim$	Implemented model
α	Void fraction

Acronyms

FWHM	Full width half max
RMSE	Root mean square error
STD	Standard deviation
WMS	Wire mesh sensors

INTRODUCTION

Radiation transmission measurements present a unique opportunity for applications to complex geometry and optically opaque systems by exploiting the principles of radiation interactions with matter. Leaping advancements in detection efficiency, spatial resolution, and high-speed acquisition systems have propelled various research fields such as the medicine, homeland security, and thermal hydraulics; the latter will be the focus of the present research. Radiation based measurements have become an essential tool in the study of multi-phase flow phenomena due to its non-intrusive nature. These phenomena present various levels of complexity due to the turbulent nature of flows, phase changes and multiphase flow interactions. The primary parameter of interest which is measured in two-phase flow phenomena is the void fraction, which describes the percent of gas-phase content in the system. The determination of this parameter is of particular importance in nuclear reactor systems in which the presence of the gas phase in the reactor core affects the reactor performance and operational safety margins [1,2].

Reported void fraction measurements using radiation transmission were performed as early as 1958 by Hooker et al. [3] and Petrick et al. [4]. Further measurements focused on nuclear reactor system applications were performed in 1965, when Sha et al. [5] used a neutron-beam to estimate the void fraction of inserts in a nuclear test section. Since then, applied radiation measurement techniques have been widely implemented in the forms of densitometry [6,7], radiography [8, 9], and computed tomography [10, 11]; these increase in spatial complexity respectively, from 1D up to 3D fields. Advanced two-phase flow instrumentation not based on radiation that are widely implemented for research include needle probes developed by Katoak et al. [12, 13] and wire-mesh sensors (WMS) developed by Prasser et al. [14]. The latter exploit the dielectric properties of liquid and gas phases to derive the local void fraction, while needle probes can be based on conductivity or optical measurements; however, both wire-mesh sensors and needle probes are intrusive, requiring the equipment to be placed in the flow field, thus causing potential perturbation of the flow. In addition, the implementation of such instrumentation is challenging at high pressures/temperatures and in complex geometries such as nuclear bundles. Radiation transmission measurement techniques instead do not suffer from these drawbacks.

The accuracy of the radiation transmission measurement of two-phase flow relies on several factors including but not limited to the detector system performance, radiation source type and strength, geometry of the experimental setup, and the transient nature of the flow; the latter is often neglected and

is the main topic of this discussion. Radiation transmission measurements of two-phase flows contain an intrinsic measurement bias which deviates the measured void fraction from the true void fraction, this is referred to as the dynamic bias. This phenomenon was first investigated by Harms et al. [15, 16], deriving expressions for simple temporal void fraction signals, exposing the magnitude that this type of bias can have on the measurement's accuracy. Andersson et al. [17], Hampel et al. [18, 19] and Wagner et al. [20] have performed additional studies using simplified temporal signals to address void fraction corrections. The present study aims to fully characterize the dynamic bias, benchmark previous research using numerical methods, adapt WMS data into hypothetical radiation transmission signals to analyze the bias magnitude for various flow regimes, and assess the effects that the bias may introduce on the measurement accuracy.

1. THE DYNAMIC BIAS ERROR

2.1 Radiation Transmission

The transmission of radiation through a medium is described by the Beers-Lambert law [21], in which an ensemble of radiation particles is exponentially attenuated due to interactions with matter; these interactions include photoelectric-absorption, Compton scattering and pair-production [22]. The next equation, is an adapted relation for radiation transmission passing through a two-phase flow system, which is analogous to the one proposed by Andersson et al. [17]

$$I_{2\varphi} = I_0\, e^{-(d_L\,\mu_L + d_G\,\mu_G) - \sum_i \mu_i \delta_i}, \qquad \text{Eq.(1)}$$

where I_0 is the radiation count rate (s^{-1}) without an object present also known as the *flat field*, d_G is the gas chord-length (m), d_L is the liquid chord-length along the radiation beam line, μ_G is the gas linear attenuation, μ_L is the liquid linear attenuation, and $\sum_i \mu_i \delta_i$ are the remainder linear attenuations and chord-lengths of additional materials in the system (i.e. pipes walls, insulators, etc.). The linear attenuation coefficient for any given material is dependent on its atomic composition, as well as the type and energy of the crossing radiation particles; this requires mindful consideration in the treatment of x-rays and neutrons which are emitted in a spectrum of energies and where the low energy particles are preferentially attenuated, thus beam hardening the particle energy spectrum. The corresponding calibration measurement for the test section completely filled with water (all-liquid system) is

$$I_L = I_0\, e^{-D\mu_L - \sum_i \mu_i \delta_i}, \qquad \text{Eq.(2)}$$

and for the test section completely filled with gas (all-gas system) is

$$I_G = I_0\, e^{-D\mu_G - \sum_i \mu_i \delta_i}, \qquad \text{Eq.(3)}$$

where D is the flow region's total chord length (i.e. pipe's inner diameter in Fig.1). During temporal two-phase flow measurements, the gas phase chord length d_G, can be described using the remainder liquid phase chord length d_L, as

$$d_G\,(t) = D - d_L(t). \qquad \text{Eq.(4)}$$

The void fraction along the chordal length is defined as

$$\alpha(t) = \frac{d_G(t)}{D}. \qquad \text{Eq.(5)}$$

The temporal void fraction $\alpha(t)$ can be any arbitrary time dependent continuous function. Based on the relations in Eq.(4) and Eq.(5), the two-phase flow radiation transmission function can be expressed in terms of the temporal void fraction as

$$I_{2\varphi}(t) = I_0\, e^{-(D[(1-\alpha(t))\mu_L + \alpha(t)\mu_G] + \Sigma_i \mu_i \delta_i)} \qquad \text{Eq.(6)}$$

This is the ideal transmission response where the attenuated intensity fluctuates based on the time dependent two-phase flow; the process is best depicted in Fig.1.

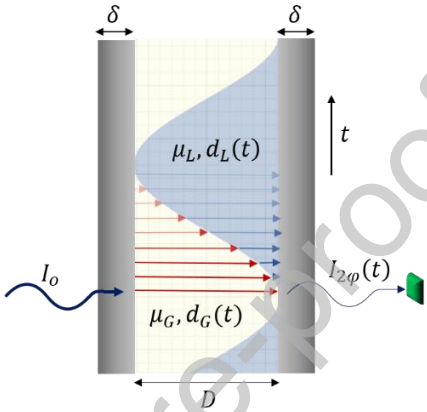

Fig.1. Radiation transmission process of a simplified time dependent two-phase flow.

Real detector systems cannot perfectly sift the radiation transmission function due to several limiting factors. Such systems require a finite integration time window in order to count radiation events. Since the detector can only sample in discretized steps, this leads to a treatment of time as a discrete sequence t_m, where the subscript m denotes the frame number in the sampling process. For convenience, time will be centered in the middle of the frame. Next, the measured detector count rate is described as a function of discrete time and detector integration period.

$$\bar{I}_{2\varphi,m}(t_m, T_d) = \frac{I_0\, e^{-\Sigma_i \mu_i \delta_i}}{T_d} \int_{a_m}^{b_m} e^{-D[(1-\alpha(\tau))\mu_L + \alpha(\tau)\mu_G]}\, d\tau. \qquad \text{Eq.(7.}a\text{)}$$

$$a_m = t_m - \frac{T_d}{2} \qquad \text{Eq.(7.}b\text{)}$$

$$b_m = t_m + \frac{T_d}{2} \qquad \text{Eq.(7.}c\text{)}$$

Here, a_m and b_m are the lower and upper time bounds of the frame, T_d is the detector frame integration period and τ is the time integration variable of the frame. The response of the detector is described here as the time average of the transmission function over a given integration window. In the case where the detector samples increasingly fast, the detector response will become the same as the ideal transmission function through the first fundamental theorem of calculus

$$\lim_{T_d \to 0} \bar{I}_{2\varphi,m}\,(t_m, T_d) \;=\; I_{2\varphi}\,(t). \qquad \text{Eq.(8)}$$

For convenience, the flow attenuation terms are consolidated into a contrast attenuation factor using the all-gas and all-liquid calibration measurements as

$$\lambda = (\mu_L - \mu_G)D = \ln\left(\frac{I_G}{I_L}\right). \quad \text{Eq.(9)}$$

This dimensionless quantity is a property of the radiation type, geometry, and two-phase flow composition which expresses the maximum contrast attenuation ranges plausible between the present phases of interest; it can represent different attenuation chord-lengths crossing the available flow geometry region (i.e. chordal paths along a circular pipe), and different types of liquid-gas mixtures described by the linear attenuation coefficients (i.e. water coolant, molten salt coolant). To give the reader some perspective, for a water-air mixture system at 20°C with a thickness D of 1 cm, paired with a standard x-ray tube at 150keV represents a $\lambda = 0.260$, and for a ^{137}Cs gamma-emitting source $\lambda = 0.086$; similarly, for a system with a thickness D of 10 cm increases the contrast attenuation factor to $\lambda = 2.165$, and $\lambda = 0.856$ respectively. It is also worth noting how x-rays are preferentially attenuated in comparison to gamma-rays; typically, gamma-ray photons are higher energy which are less likely to interact with matter than the lower energy medical x-ray photons.

After the two-phase flow measurement is performed, the signal is post processed by transforming the measurement from recorded transmission counts to void fraction; this requires dividing the measurement in Eq.(7.a) by the liquid calibration in Eq.(2), taking the natural logarithm and dividing by Eq.(9) as

$$\alpha_{s,m}(t_m, T_d, \lambda) = \frac{1}{\lambda}\ln\left(\frac{I_0 e^{-(D\mu_L + \sum_i \mu_i \delta_i)}}{I_L T_d}\int_{a_m}^{b_m} e^{\lambda\alpha(\tau)}\, d\tau\right); \quad \text{Eq.(10)}$$

the subscript s is used here to denote the sampling process of the void fraction. The division by the all-liquid calibration measurement eliminates the liquid and external material attenuation terms which are also found in the two-phase flow transmission function. With further simplifications of Eq.(10) allows us to estimate the sample average void fraction from the temporally collected frames

$$\bar{\alpha}_s(T_d, \lambda) = \frac{1}{M}\sum_{m=1}^{M}\left[\frac{1}{\lambda}\ln\left(\frac{1}{T_d}\int_{a_m}^{b_m} e^{\lambda\alpha(\tau)}\, d\tau\right)\right], \quad \text{Eq.(11)}$$

where M is the total number of frames or recorded measurements. The sample average void fraction shows that the averaging procedure should be performed after the logarithmic conversion in Eq.(11), Hampel [18] refers to this as the correct averaging method, supported in the limit where the integration period becomes significantly small, as described in Eq.(8). On the contrary, when the detector integration window becomes increasingly large, temporal averaging occurs during the actual measurement integration period, thus happening inside the logarithmic function in Eq.(11); this results in an erroneous averaging procedure.

2.2 The Dynamic Bias

The dynamic bias emerges as a result of the inexact averaging procedure previously discussed; the bias is defined as the deviation or absolute error of the sampled void fraction ($\alpha_{s,m}$) in comparison to the true void fraction. Let us first define the instantaneous frame bias as

$$\Delta\alpha(t_m, T_d, \lambda) = \frac{1}{\lambda}\ln\left(\frac{1}{T_d}\int_{a_m}^{b_m} e^{\lambda\alpha(\tau)}\, d\tau\right) - \frac{1}{T_d}\int_{a_m}^{b_m}\alpha(\tau)\, d\tau. \quad \text{Eq.(12)}$$

The dynamic bias becomes the average accumulation of error over the range of the instantaneous frames throughout the measurement; this is expressed as

$$\Delta\alpha(T_d, \lambda) = \frac{1}{M}\sum_{m=1}^{M}\left[\frac{1}{\lambda}\ln\left(\frac{1}{T_d}\int_{a_m}^{b_m} e^{\lambda\alpha(\tau)}\, d\tau\right) - \frac{1}{T_d}\int_{a_m}^{b_m}\alpha(\tau)\, d\tau\right]. \quad \text{Eq.(13)}$$

This type of error occurs due to the fact that the natural log of the measurement is applied on the outside of the integral operation, therefore it occurs as the acquisition window is extended which results in a deviation from the behavior of the sampled function. Now, changing variables allows the sampling integration period to be defined relative to the two-phase flow phenomena period, removing the need to stipulate a specific period, but conveniently describing how one scales relative to the other:

$$T_d = \beta\, T_\alpha, \quad \text{Eq.(14.}a\text{)}$$

$$f_d = \frac{f_\alpha}{\beta}, \quad \text{Eq.(14.}b\text{)}$$

$$\beta = \frac{T_d}{T_\alpha} = \frac{f_\alpha}{f_d}. \quad \text{Eq.(14.}c\text{)}$$

Here, T_α is the ideal void fraction phenomena period, f_α is the corresponding ideal phenomena frequency, T_d is the detector sampling time period and f_d is the corresponding detector sampling frequency. The parameter β can characterize the transition from the proper to the wrongful averaging implementation. When $\beta < 1$, the sampling is occurring faster than the phenomena frequency, nevertheless, one should sample at $\beta < 0.5$ following the Nyquist criterion to capture time resolved information of the phenomena. When $\beta > 0.5$ results in a time average beyond the Shannon-Nyquist criterion, thus failing to capture temporal information, instead becoming a measure of the average behavior of the flow. The dynamic bias buildup from Eq.(13) can then be rewritten using the new relations as

$$\Delta\alpha(\beta, \lambda) = \frac{1}{M}\sum_{m=1}^{M}\left[\frac{1}{\lambda}\ln\left(\frac{1}{\beta\, T_\alpha}\int_{a_m}^{b_m} e^{\lambda\alpha(\tau)}\, d\tau\right) - \frac{1}{\beta\, T_\alpha}\int_{a_m}^{b_m}\alpha(\tau)\, d\tau\right]. \quad \text{Eq.(15)}$$

This expression will be used to numerically evaluate the dynamic bias associated to an arbitrary temporal two-phase flow functions being measured by a hypothetical radiation detection system.

2.3 Variance Effects on the Dynamic Bias

The dynamic bias is also strongly dependent on the gas fraction fluctuations of the true void fraction $\alpha(t)$ function, this will be referred as the void fraction amplitude throughout the text; as one can imagine, abrupt and irregular behavior could heavily influence the buildup of this error. If a time-resolved experimental signal is analyzed in steady-state conditions, it basically consists of a fluctuation around the true mean value $\bar{\alpha}$, which can be obtained by means of time averaging given a time frame T_α. However, the characteristic amplitude of such random-like oscillation influences the dynamic bias. Square-like

signals can be taken as a reference so that a general approximation can be obtained to estimate the dynamic bias. Let us first derive a generalized expression based on rectangular pulse signals whose void fraction is composed of an active and passive phase components, as shown in the examples of Fig.2. Throughout the text, the active portion is considered as the components of the signal that are above the average, similarly, the passive portion is considered as those below the average and represent a void fraction baseline, or lack thereof. The temporal distribution or in this case the duty cycle ω represents the portion of time for which the void fraction is active over the phenomena cycle T_α, this can be expressed as

$$\omega = \frac{\tau^+}{T_\alpha}, \qquad \text{Eq.(16.}a\text{)}$$

and the passive portion of the time is described as

$$(1-\omega) = \frac{\tau^-}{T_\alpha}. \qquad \text{Eq.(16.}b\text{)}$$

Here τ^+ and τ^- represent the signal's active and passive duration. The active and passive amplitudinal displacements away from the mean void fraction are $\varepsilon^+$and ε^- respectively. The signal variance is an important parameter of interest which characterizes the signal fluctuation, however, this parameters is obtained with time resolved measurements. The analytical variance of the square signal is defined as

$${\sigma_\alpha}^2 = \omega(\varepsilon^+)^2 + (1-\omega)(\varepsilon^-)^2. \qquad \text{Eq.(17)}$$

This involves respectively weighting the squared active and passive amplitudes by the corresponding temporal portion described in Eq.(16.a). The dynamic bias can be modified from Eq.(15) for a square signal with a single measurement cycle assuming M = 1 and an acquisition to phenomena period ratio of $\beta = 1$, the expression is then simplified through the following

$$\Delta\alpha(T_\alpha, \tau^\pm, \varepsilon^\pm, \lambda) = \frac{1}{\lambda}\ln\left(\frac{1}{T_\alpha}\int_0^{\tau_i^+} e^{\lambda(\bar{\alpha}+\varepsilon^+)}\,d\tau + \frac{1}{T_\alpha}\int_{\tau_i^+}^{\tau_i^+ + \tau_i^-} e^{\lambda(\bar{\alpha}-\varepsilon^-)}d\tau\right) - \bar{\alpha}, \qquad \text{Eq.(18.}a\text{)}$$

with some algebraic manipulation and using the substituting in the relations from Eq.(16.a), the dynamic bias becomes

$$\Delta\alpha(\omega, \varepsilon^\pm, \lambda) = \frac{1}{\lambda}\ln\left(\omega e^{\lambda\varepsilon^+} + (1-\omega)e^{-\lambda\varepsilon^-}\right). \qquad \text{Eq.(18.}b\text{)}$$

This final expression describes the dynamic bias for any parametrized square signal. It is worth pointing out that Eq.(18.b) reveals that the dynamic bias is dependent on the temporal distribution and amplitude displacements between the active and passive components of the signal and is independent on the average void fraction of the signal; this implies that the dynamic bias is shift invariant.

Now let us consider a symmetric square signal as shown in Fig.2*a*; for reference, symmetric in this case describes equal temporal and amplitudinal distributions between the active and passive components of the signal; the assumptions for this particular case then implies:

$$\omega = (1-\omega) = \frac{1}{2}, \qquad \text{Eq.(19)}$$

$$\varepsilon^+ = \varepsilon^- = \varepsilon\,. \qquad \text{Eq.(20)}$$

It can then be easily proven that the standard deviation σ_α is equivalent to the amplitudinal components by replacing the relations of Eq.(19) and Eq.(20) into the expression in Eq.(17) which simplifies to.

$$\sigma_\alpha = \varepsilon \qquad \text{Eq.(21)}$$

The dynamic bias from Eq.(18.b) can now be expressed in terms of the signal's standard deviation

$$\Delta\alpha(\sigma,\lambda) = \frac{1}{\lambda}\ln\left(\frac{e^{\lambda\sigma_\alpha} + e^{-\lambda\sigma_\alpha}}{2}\right) = \frac{1}{\lambda}\ln[\cosh(\lambda\sigma_\alpha)], \qquad \text{Eq.(22)}$$

which is the same expression proposed by Harms et al. [16] following an analogous derivation. In addition, the expression in Eq.(22) is expanded with the Maclaurin series based on $\lambda\sigma_\alpha$ as the independent variable,

$$\frac{1}{\lambda}\ln[\cosh(\lambda\sigma_\alpha)] = \frac{\lambda}{2}\sigma_\alpha^2 - \frac{\lambda^3}{12}[\sigma_\alpha^2]^2 + \cdots \qquad \text{Eq.(23)}$$

where it can be observed that if the value of σ_α is small enough, the linear term with respect to σ_α^2 is the only relevant portion. Therefore, the dependence of the dynamic bias and the signal's variance σ_α^2 is virtually linear.

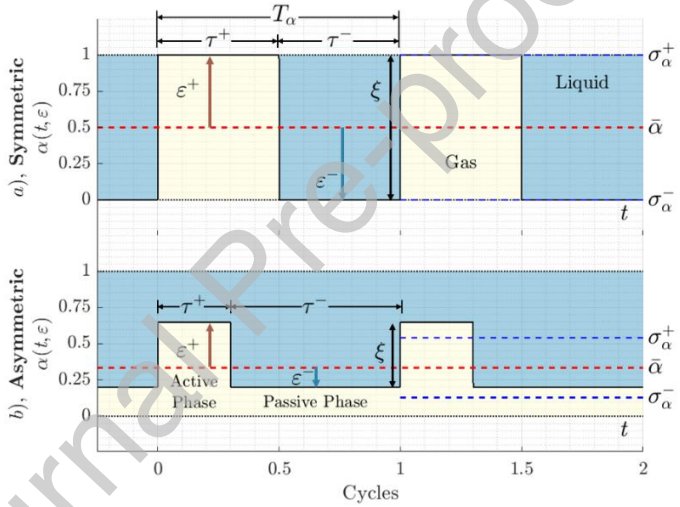

Fig.2. Example of *a)* symmetric and *b)* asymmetric square signals.

Now let us consider an asymmetric periodic square signal with unbalanced temporal and amplitudinal distributions between the active and the passive phases with an arbitrary example shown in Fig.2*b*. The active and passive amplitudinal displacements of the signal can now be defined in terms of the signal variance and the temporal distribution

$$\varepsilon^+ = \sqrt{\frac{\sigma_\alpha^2(1-\omega)}{\omega}}, \qquad \text{Eq.(24.}a\text{)}$$

$$\varepsilon^- = \sqrt{\frac{\sigma_\alpha^2\,\omega}{(1-\omega)}}. \qquad \text{Eq.(24.}b\text{)}$$

The peak-to-peak amplitude of the signal is described as the sum of the active and passive amplitude displacements of the signal

$$\xi = \varepsilon^+ + \varepsilon^-, \qquad \text{Eq.(25.}a\text{)}$$

$$\xi = \sqrt{\frac{\sigma_\alpha^2}{(1-\omega)\omega}}. \qquad \text{Eq.(25.}b\text{)}$$

The peak-to-peak amplitude ξ has a plausible range between 0 and 1; the expression in Eq.(25.b) allows us to substitute between the signal variance and the peak-to-peak amplitude depending on which one is more convenient. The dynamic bias can alternatively be expressed in terms of ξ or σ_α^2 by algebraically rearranging Eq.(18.b) as

$$\Delta\alpha(\omega,\xi,\lambda) = \frac{1}{\lambda}\ln\left(\omega + (1-\omega)e^{-\lambda\xi}\right) + \xi(1-\omega) \qquad \text{Eq.(26.}a\text{)}$$

$$\Delta\alpha(\omega,\sigma_\alpha^2,\lambda) = \frac{1}{\lambda}\ln\left(\omega + (1-\omega)e^{-\lambda\sqrt{\frac{\sigma_\alpha^2}{(1-\omega)\omega}}}\right) + \sqrt{\frac{\sigma_\alpha^2(1-\omega)}{\omega}}. \qquad \text{Eq.(26.}b\text{)}$$

These expressions are equivalent and describe the corresponding dynamic bias of a system characterized by λ, a temporal distribution ω, the peak-to-peak amplitude ξ, and whose variance is σ_α^2; which estimates the bias for the set of conditions which describe the signal. The most direct way to see the advantages of this proposed model Eq.(26.b) is to compare it with the expression proposed by Harms in Eq.(22). The latter has only two parameters to characterize the signal. However, when studying signals from two-phase flow, the different flow patterns have a non-symmetrical time distribution between the two phases as will be shown in Fig.16*c* in section 4.5; the experimental results will depict that ω is significantly dependent on the flow regime. In reality, the condition ω=0.5 to which Harms's model is constrained cannot be guaranteed. Alternatively, the proposed expression in Eq.(26.b) incorporates the third parameter ω that accounts for the temporal asymmetry information that was previously missing. By having this additional third parameter, the prediction becomes more accurate, however, this third parameter implies greater complexity in the prediction since ω value must be approximated.

The 3D diagram of the dynamic bias is depicted in Fig.3*a* as a function of the possible values of ω and λ, and where the condition of ξ =1 defines the outermost boundary of the volume; the superimposed color corresponds to the duty cycle and the planes are examples of a 1cm thick water-air system at 20°C paired with 150 keV x-ray and ^{137}Cs radiation sources. The cross-sectional slice shown in Fig.3*b* corresponds to the example plane for $\lambda = 2$. This highlights the inner region of the volume in which the grid denotes the parabolic isolines corresponding to constant peak-to-peak amplitude ξ and the vertical isolines corresponding to constant duty cycle ω. The cross-section exhibits a skewing behavior towards low void fraction range, in particular with the increase of λ.

Similarly, the 3D diagram of the dynamic bias as a function of the possible values of ${\sigma_\alpha}^2$ and λ is presented in Fig.3*c*. The dynamic bias grows in a predominantly linearly fashion for small values of λ and can be best predicted following the expression Eq.(23) in this region, however, the error unfolds to an elliptical shape with increased λ; the latter is best depicted by the cross-sectional slice corresponding to $\lambda = 2$ shown in Fig.3*d*. The elliptical slice can be described as a series of concentric shells corresponding to the peak-to-peak isolines ξ. The upper portion of the shell correlates to $0 \leq \omega < \frac{1}{2}$, the bottom correlates to $\frac{1}{2} < \omega \leq 1$, and these converge to Eq.(22) when $\omega = \frac{1}{2}$. The physical connotation implies that a short burst signal has a larger embedded error than a signal of longer duration, for signals

characterized by the same variance. This also entails that for the prior case, the passive phase is dominant, which contains the largest amount of liquid, representing a higher attenuation medium. In the latter case, the active phase is dominant, which contains a significantly larger amount of gaseous phase constituting a lower attenuation medium that yields a lower dynamic error.

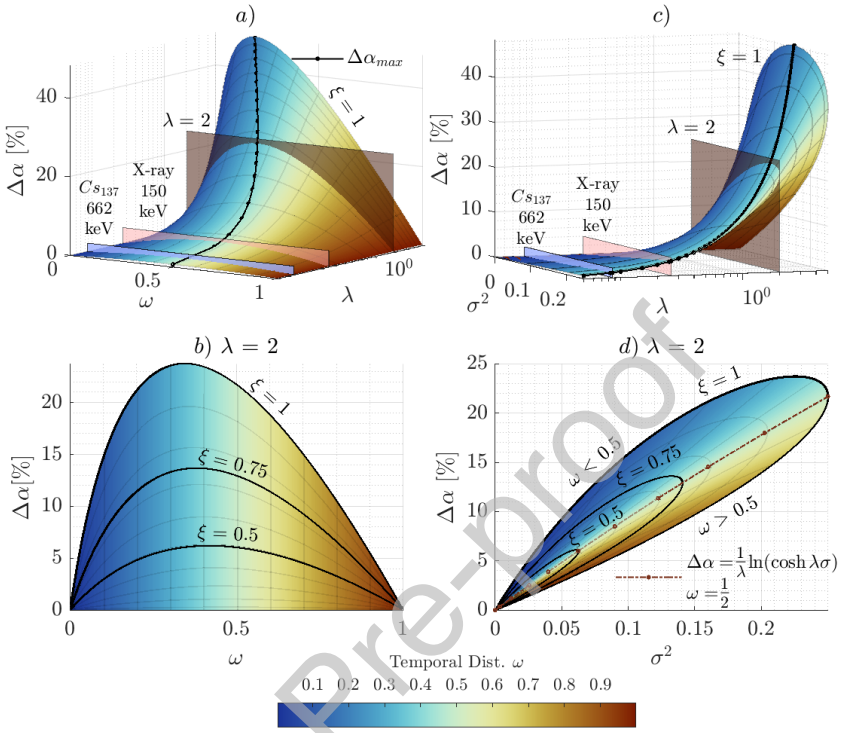

Fig.3. Dynamic bias of the Rect function *a)* as a function of ω and λ with planes representing x-ray and gamma-ray system for 1 cm thickness, *b)* cross-sectional slice as a function of ω for $\lambda = 2$. *c)* as a function of ${\sigma_\alpha}^2$ and λ, *d)* cross-sectional slice as a function of ${\sigma_\alpha}^2$ for $\lambda = 2$.

The parabolic shape of the dynamic bias shown in Fig.3*a* indicates that there is a maximum value which corresponds to a critical duty cycle. This can be solved by differentiating Eq.(26.a) in terms of the duty cycle ω as

$$\frac{\partial \Delta\alpha}{\partial \omega} = \frac{e^{\lambda\xi} - 1}{\lambda + (e^{\lambda\xi} - 1)\lambda\omega} - \xi. \qquad \text{Eq.(27)}$$

Setting the derivative to zero allows us to solve for the critical duty cycle corresponding to the maximum dynamic bias for a given contrast attenuation factor and peak-to-peak amplitude,

$$\omega_{cr} = \frac{e^{\lambda\xi} - \lambda\xi - 1}{\lambda\xi(e^{\lambda\xi} - 1)}. \qquad \text{Eq.(28)}$$

The evolution of the maximum dynamic bias as a function of λ is obtained by inputting the critical duty cycle ω_{cr} from Eq.(28) into Eq.(26.a) for $\xi = 1$; this is depicted by the superimposed black line of Fig.3*a*, and the evolution of the maximum value is shown in Fig.4*a*. The results reinforces the linear behavior of the error for small values of λ, as well as its deviation from linearity with increased λ. The critical duty cycle ω_{cr} starts at 0.5 and rapidly decreases shown in Fig.4*b*, which symbolizes the tendency of the bias

to be preferentially larger for short duration signals with a dominant passive-phase; when $\xi = 1$ represents an all-liquid passive phase.

The critical variance is obtained by solving Eq.(25.b) in terms of the variance and plugging in the critical duty cycle,

$$\sigma_{\alpha_{cr}}^2 = \xi^2(\omega_{cr} - {\omega_{cr}}^2). \qquad \text{Eq.(29)}$$

The evolution of the critical variance corresponding to the maximum dynamic bias is shown Fig.4*b*; it presents an initially slow decline which becomes linear with increased λ. The critical variance described by Eq.(29) is influenced by values where $\omega_{cr} < 1/2$, which is consistent with what has been observed. The analytical expression derived of the dynamic bias from the rectangular pulsed signal serves as a framework for the improved modeling and understanding of said phenomenon.

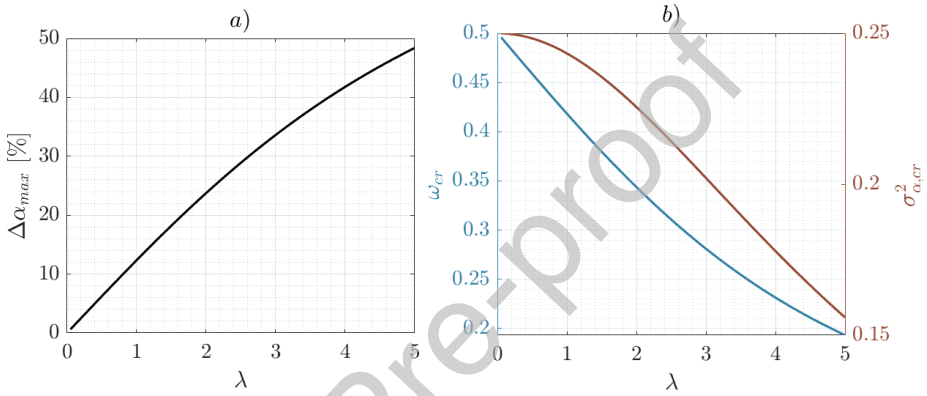

Fig.4. *a)* evolution of maximum dynamic bias as a function of λ. *b)* critical duty cycle (left) and corresponding critical variance (right) as a function of λ.

2. SIMPLIFIED SIGNALS

The dynamic bias is an unavoidable effect intrinsic to radiation measurements of temporal signals. This section will focus on the numerical modeling of the dynamic bias for simplified void fraction signals to gain intuition of its behavior. Simplified signals can give insight into how the dynamic bias varies as a function of integration window, contrast attenuation factor, and imposed void fraction. These parameters are influenced by several experimental conditions including but not limited to:

- Frame rate limitation of the detector.
- Operation below the counting saturation limit of the detector counters.
- Radiation source strength: weak radiation sources require long integration periods of time to obtain statistically significant results.
- Experiments with high-attenuation materials (i.e. insulators, pipe walls) effectively reduce the radiation flux available which can also result in longer integration periods of time.
- Type of radiation and atomic composition of the liquid and gas phases which determine the contrast attenuation factor.

3.1 Numerical Modeling

The present study aims to validate the dynamic bias model based on well-behaved void fraction signals, in this section we will use rectangular, sinusoidal, and triangular pulses for these purposes; these signals are ordered in descending temporal gradient complexity and will be respectively referred to as Rect, Sine, and Tri functions throughout the text. These signals serve as ideal models used to first understand the dynamic bias; however, real life signals are random in nature resulting in an erratic behavior in comparison to the ones that will be utilized. The signals are built by manipulating the duty cycle ω or full width half max (FWHM) of the pulsed shape, the imposed peak-to-peak amplitude ξ has a value of 1 given that this defines the outer limit of the dynamic bias volume as was observed in the previous section. The generated signals serve as inputs to a custom-built script that numerically evaluates Eq.(13); the data analysis scripts, and other functions were developed in MATLAB® 2019b.

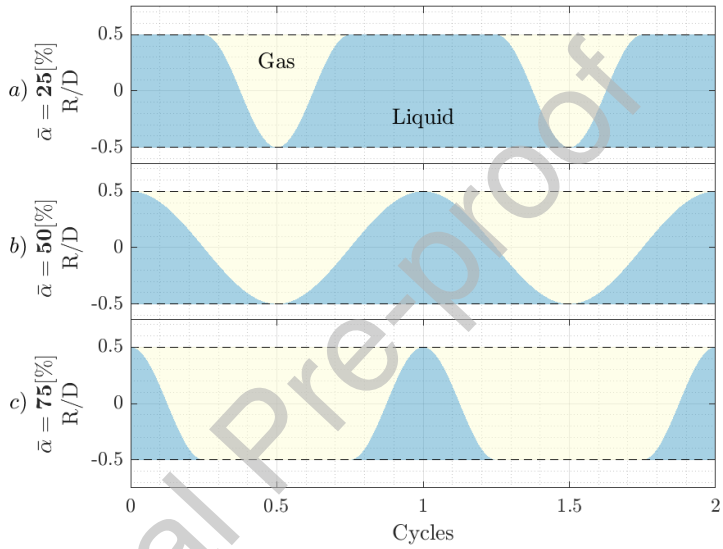

Fig.5. Example of sinusoidal with modified duty cycle modulation for *a)* 25%, *b)* 50%, and *c)* 75% average void fraction.

The Rect function was characterized in the previous section, this function represents the most extreme case in which the phase changes occur abruptly, while the triangular function steadily shifts the balance between the phases. The sinusoidal function represents an intermediate behavior between the prior two other functions. The temporal duration of the pulse is fitted to yield the desired average void fraction in a cycle; this will be referred as the pulse duty cycle modulation method. The implemented definitions of the Tri and Sine functions can be found in the Appendix. An illustrative example of the modified Sine signal is shown in Fig.5 for 25%, 50%, and 75% imposed average void fraction; the 25% and the 75% void fraction signals contain equivalent variance. The 50% void fraction signal will be first used to compare the dynamic bias model with the literature.

The geometric and material parameters such as pipe diameter, liquid, and gas linear attenuations used in this subsection are based on the study performed by Andersson et al. [17] which modeled a neutron radiation system with two-phase flow at 80 bars of pressure. The reported pipe diameter is 25 mm, the liquid attenuation is 7.2E-3 mm^{-1}, and the gas attenuation is 3.6E-4 mm^{-1}; this is equivalent to a contrast attenuation factor of λ = 0.173. For this study, the signals had an imposed average void fraction of 50%

and were carried out over 50 phenomena cycles. The numerical standard deviation of the simulated signal's true void fraction is expressed with the following

$$\sigma_\alpha = \sqrt{\frac{1}{M}\sum_{m=1}^{M}(\alpha_m - \bar{\alpha})^2} \quad \text{Eq.(30)}$$

where α_m is the ideal void fraction sampled over the frame m, and $\bar{\alpha}$ is the signal's true average void fraction. Similarly, the standard deviation of the dynamic bias is defined with the following

$$\sigma_{\Delta\alpha} = \sqrt{\frac{1}{M}\sum_{m=1}^{M}(\Delta\alpha_m - \Delta\bar{\alpha})^2}, \quad \text{Eq.(31)}$$

which describes the spread of the instantaneous frame errors in comparison to the average error buildup. The dynamic bias results for the three modeled functions are shown in Fig.6*a*. The instantaneous realizations of the dynamic bias described by Eq.(12) are depicted as scatter dots; these illustrate the aliasing lobes that arise from the mismatched sampling frequencies and the phenomena frequency, with nodes located where the phenomena frequency is divisible by the sampling frequency. The buildup curves described by Eq.(15) increase in the region where β < 1, these then stabilize in the region where β > 1 with dampening oscillations and asymptotically converging due to the increased average integration window. For this case, the asymptotic value of the Rect function is 2.14%, the Sine function is 1.07%, and for the Tri function is 0.71%. These results match the values reported by Andersson et al. [17] for the Rect with a difference of 0.04% and the Sine function with negligible difference; the small sources of difference may arise due to noise incorporation in the referenced study. The results also show that the Rect function has the largest dynamic bias, the Sine has the second largest and the Tri function has the smallest. This occurs because the Rect function has the most abrupt transitions between phases as previously mentioned. The instantaneous realizations also show the variation of dynamic bias which is best described by its standard deviation expressed in Eq.(31) and shown in Fig.6*b*. The dynamic-bias standard deviation is depicted as a series of lobes that are damped due to the increased averaging that occurs with increase in β, with the largest lobe occurring where $0 < \beta < 1$. The standard deviation of the true window averaged void fraction described by Eq.(30) is plotted in Fig.6*c* as a function of β. This also exhibits a dampening lobe behavior, as β approaches zero representing an ideally fast sampling system, the true void fraction's standard deviation converges on to the function's analytical standard deviation, with values of 50% for the Rect function, 35.6% for the Sine function, and 28.9% for the Tri function; the latter two results can be verified using Eq.(B.3.b) and Eq.(A.3.b) respectively. When performing time resolved measurements, one should maintain the sampling rate below the Nyquist criterion as previously postulated, therefore sample at least at twice the phenomena frequency, nevertheless it becomes clear that there is an inherit bias error from the measurements which is decreased but not entirely eliminated at high sampling rates, unless the flow appears completely stationary during the measurement period.

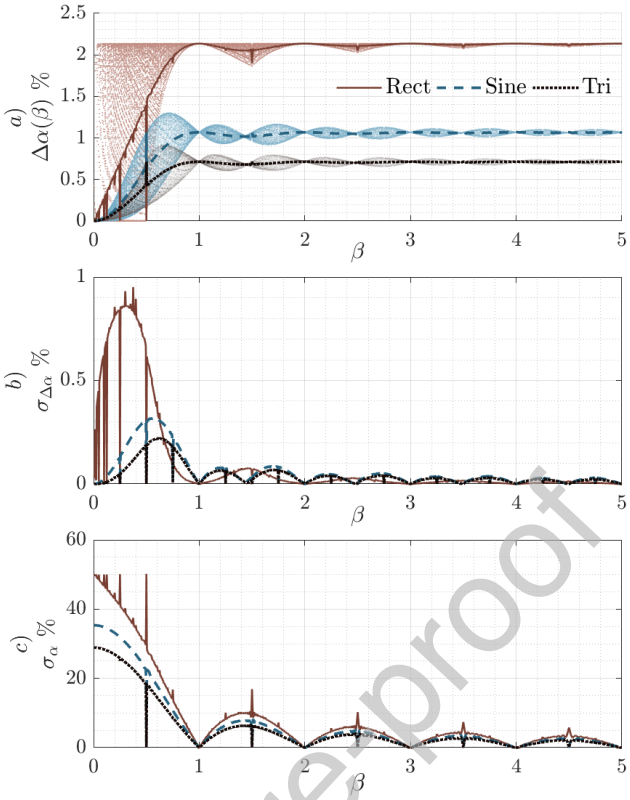

Fig.6. *a)* Dynamic bias curve buildup, *b)* dynamic bias standard deviation, and *c)* true void fraction standard deviation for 50% imposed void fraction.

3.2 Pulse Duty Cycle Modulation Study

The dynamic bias parametric study was conducted by implementing the duty cycle modulation approach, the average void fraction $\bar{\alpha}$ was systematically increased from 0.2% to 99.8% in steps $\Delta\bar{\alpha}$ of 0.2%. The contrast attenuation factor λ values used were varied from 0.01 to 3 in incremental steps $\Delta\lambda$ of 0.01, the peak-to-peak amplitude was maintained as $\xi = 1$, and $\beta = 1$ was used to assume a detector integration period equivalent to the signals period. The results presented in Fig.7 depict the dynamic bias as a function of the imposed average void fraction and contrast attenuation factor for the three functions. The dynamic bias of the Rect function exhibits a skewed behavior leaning towards the low void fraction range; this is supported in Sec. 2.3 and the analytical results validate the numerical model implemented in this study. The Sine and the Tri functions have two peaks with a cusp located along the void fraction value of 50%; this is due to the piecewise definition of the functions used to build the signals. The tendency shows that the low void fraction peak is larger for both functions.

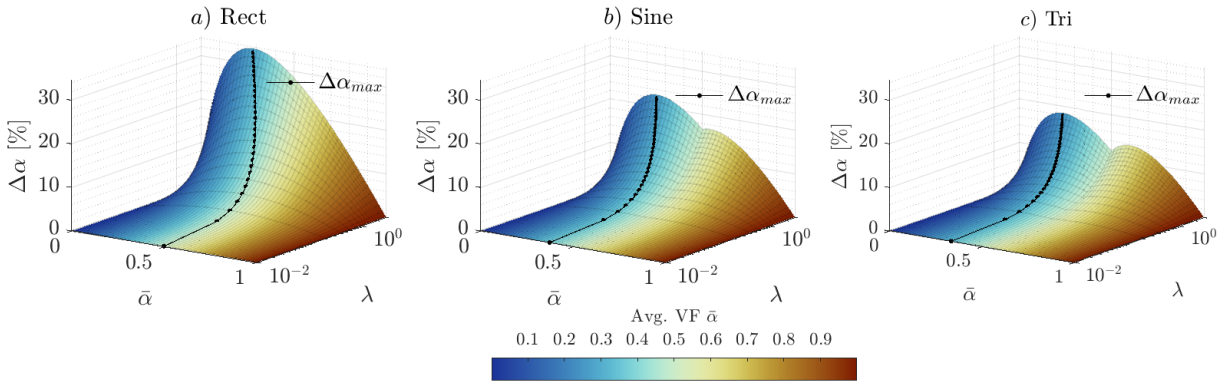

Fig.7. Dynamic bias as a function of imposed average void fraction and contrast attenuation factor. *a)* Rect, *b)* Sine, and *c)* Tri functions.

The dynamic bias plotted against the variance of the original signal is shown in Fig.8, *a*) for λ = 1, and *b*) for λ = 2. The results further confirm the analytical expression derived from the Rect function in Eq.(26.b). Although the Rect function exaggerates the abrupt phase change, it traces the boundary for the maximum possible error as a function of the true signal variance. The Sine and Tri functions present similar elliptical behaviors overall contained within the Rect functions range. The results reaffirm that signals with equal variance but with dominant liquid phase, lead to higher accumulations of error. Experimental facilities with large contrast attenuation factors are more susceptible to these types of embedded errors, therefore it is important to estimate this factor to scale the dynamic bias appropriately. The Rect function can be used as a conservative and slightly exaggerated measure of the maximum dynamic bias error; this can be estimated for a given experimental setup by calculating the critical duty cycle as defined in Eq.(28) and plug it into Eq.(26.a) for a peak-to peak amplitude $\xi = 1$.

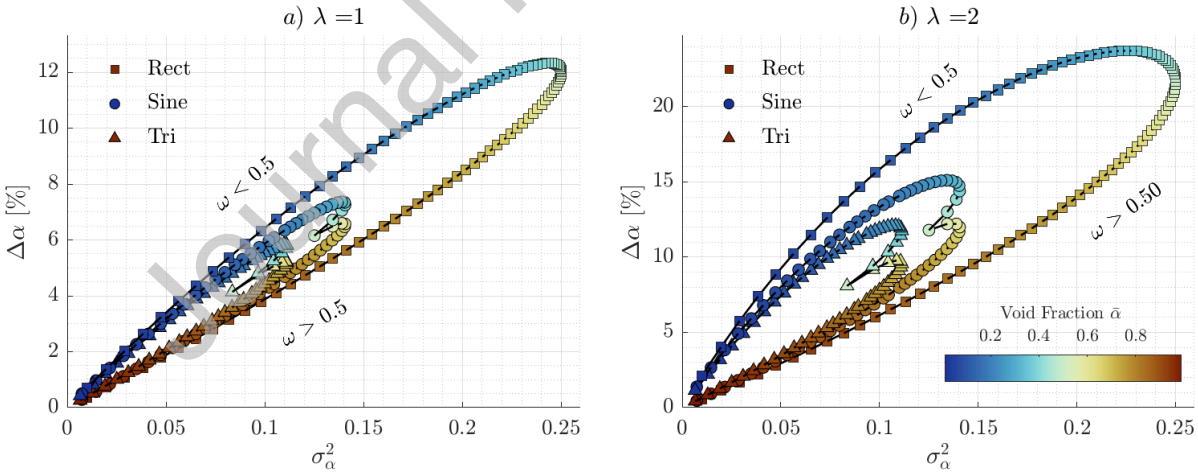

Fig.8. Dynamic bias relation to the variance of the true void fraction for the three simplified signals. *a)* λ = 1, and *b)* λ = 2 contrast attenuation factor.

3.3 Temporal Distribution Model

The analytical expression of the dynamic bias derived from the rectangular pulse provides a framework which could be used to better predict the error for an arbitrary signal. To achieve this, we propose the temporal distribution model which aims to estimate the dynamic bias by simplifying an arbitrary signal

into an active and passive phase component from an approximated temporal distribution, while preserving the average void fraction and signal variance. In this study, we decided to calculate the amplitudinal centroids of the signal's active and passive components, and from these, estimate the temporal distribution ω. This requires the signal to be mean centered, therefore one must subtract the average value of the signal and split it into positive and negative parts as follows

$$\alpha(\tau)^+ = \begin{cases} \alpha(\tau) - \bar{\alpha} & \text{if } \alpha(\tau) - \bar{\alpha} > 0 \\ 0 & \text{otherwise} \end{cases}, \quad \text{Eq.(32.}a\text{)}$$

$$\alpha(\tau)^- = \begin{cases} \bar{\alpha} - \alpha(\tau) & \text{if } \alpha(\tau) - \bar{\alpha} < 0 \\ 0 & \text{otherwise} \end{cases}, \quad \text{Eq.(32.}b\text{)}$$

where $\pm$ defines the polarity of the component. The positive and negative areas of the mean centered signal are respectively defined as

$$A^+ = \int_0^{T_d} \alpha(\tau)^+ \, d\tau, \quad \text{Eq.(33.}a\text{)}$$

$$A^- = \int_0^{T_d} \alpha(\tau)^- \, d\tau \quad \text{Eq.(33.}b\text{)}$$

The centroids of the positive and negative portions of the signal are then estimated as

$$\Theta^+ = \frac{1}{A^+} \int_0^{T_d} \frac{1}{2} [\alpha(\tau)^+]^2 \, d\tau, \quad \text{Eq.(34.}a\text{)}$$

$$\Theta^- = \frac{1}{A^-} \int_0^{T_d} \frac{1}{2} [\alpha(\tau)^-]^2 \, d\tau. \quad \text{Eq.(34.}b\text{)}$$

The amplitude centroids define the active and passive component's weight-like center and their separation with respect to the mean. The temporal distribution can then be estimated as a weighted quantity, in which the negative centroid Θ^- is divided by the sum of both centroids.

$$\omega_{cent} = \frac{\Theta^-}{\Theta^+ + \Theta^-}. \quad \text{Eq.(35)}$$

This estimates the balance that exists between the active and the passive phase of the signal, therefore if the signal is temporally asymmetric as shown in Fig.2*b*, in which one phase has a longer duration, then this will be reflected in the centroid separation with respect to the mean. In the opposite case where the signal is temporally symmetric as shown in Fig.2*a*, then the centroid separation will be equivalent and $\omega_{cent} = 1/2$. In addition, the amplitudinal components can be estimated with the relations presented in Eq.(24.a) through Eq.(25.b) which depend on σ_α^2 and ω_{cent}. This model allows us to reduce an intricate signal into an equivalent rectangular distribution. As a proof of concept, it is important to verify that this method solves the case of the rectangular pulsed signal. The positive and negative parts of a mean centered rectangular signal can be defined as

$$\alpha(\tau)_{Rect}^+ = \begin{cases} \varepsilon^+ & \text{if } \alpha(\tau) - \bar{\alpha} > 0 \\ 0 & \text{otherwise} \end{cases}, \quad \text{Eq.(36.}a\text{)}$$

$$\alpha(\tau)_{Rect}^- = \begin{cases} \varepsilon^- & \text{if } \alpha(\tau) - \bar{\alpha} < 0 \\ 0 & \text{otherwise} \end{cases}. \quad \text{Eq.(36.}b\text{)}$$

These can then be used to evaluate the respective centroids defined in Eq.(34.a) which yield the following

$$\Theta^{+}_{Rect} = \frac{\varepsilon^{+}}{2}, \qquad \text{Eq.(37.}a\text{)}$$

$$\Theta^{-}_{Rect} = \frac{\varepsilon^{-}}{2}. \qquad \text{Eq.(37.}b\text{)}$$

These definitions can be plugged into Eq.(35), and the temporal distribution for a Rect function is then expressed as

$$\omega_{Rect} = \frac{\varepsilon^{-}}{\varepsilon^{+} + \varepsilon^{-}}. \qquad \text{Eq.(38)}$$

Alternatively and in a straightforward manner, the temporal distribution can be solved by equating the positive and negative areas respectively above and below the mean,

$$0 = \ \omega\varepsilon^{+} - \ (1-\omega)\varepsilon^{-}. \qquad \text{Eq.(39)}$$

and solving for the temporal distribution results in the same expression as in Eq.(38). Although the proof of concept is simple in nature, it shows that the centroid estimation method appropriately estimates the temporal distribution of a rectangular function. However, the goal is to approximate ω for any arbitrary function. The dynamic bias can then be estimated from Eq.(26.b) based on the signal variance σ_{α}^{2} and the obtained value of ω.

In practice, the dynamic bias was typically calculated using the expression in Eq.(22) originally derived by Harms [16] which only requires the signal's variance as an input. Nevertheless, this expression considered symmetry of the amplitudinal displacement in relation to the mean and neglects the influence that the temporal distribution has on the dynamic bias. In contrast, the proposed model now incorporates the temporal aspect to predict this error more accurately. The temporal distributions of the previously modulated signals were estimated using the centroid method, the dynamic bias was then calculated using Eq.(26.b). Next, we subject Harms's model and the proposed model to a 1:1 comparison in relation to the ideal error, this is assessed for the three types of signals using a contrast attenuation value of $\lambda = 2$. The results of Harms's model are plotted against the true dynamic bias in Fig.9*a*; ideally, the prediction should lie close to the identity line. Similarly, the 1:1 comparison of the ideal and the proposed model is depicted in Fig.9*b*. The results show that Harms's predictive model broadly deviates away from the identity line for all three signal types, while the proposed model closely maps the results of the triangular and sinusoidal signals along the identity line, and the results from the rectangular signals match perfectly as it would be expected. Moreover, the models accuracy can be further evaluated by estimating the root mean square error (RMSE); this parameter quantifies the predictive power of a model in relation to the data samples. We will define the RMSE as

$$RMSE \ = \ \sqrt{\frac{1}{N}\sum_{n}^{N}(\Delta\tilde{\alpha}_{n} \ - \ \Delta\alpha_{n})^{2}}, \qquad \text{Eq.(40)}$$

where $\Delta\tilde{\alpha}$ denotes the implemented model, $\Delta\alpha_{n}$ is the ideal dynamic bias, and n denotes the data points in each signal type analyzed. The RMSE was evaluated for various values of λ given that the error increases with this parameter. The results of the three functions are depicted in Fig.10, this reflect how the predictability of Harms's model degrades rapidly with increased λ, while the proposed model remains

within 1% for values of λ as large as 3. It is worth mentioning that the proposed model yields an RMSE of zero for the Rect function, meaning that it perfectly estimates the bias for this signal type since it is the basis of the model.

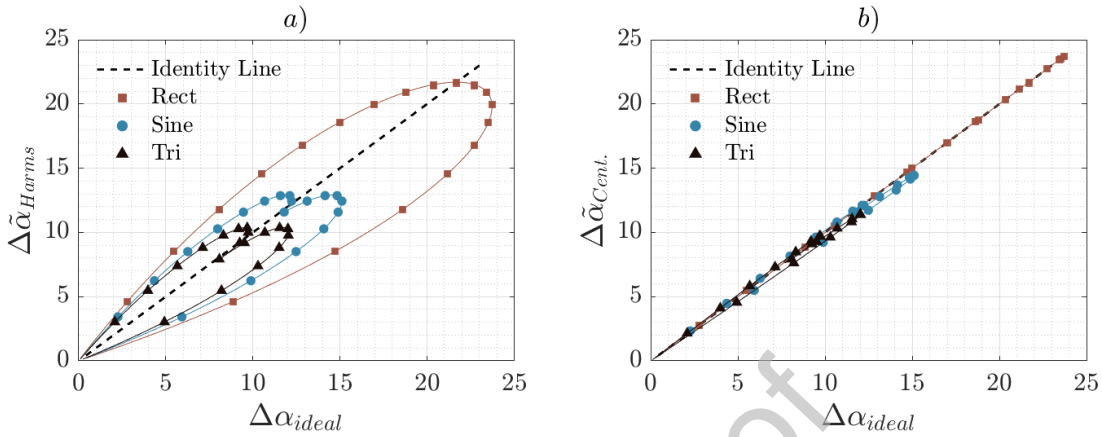

Fig.9. One to one comparison of the ideal dynamic bias with value predicted for *a)* Harms model, and *b)* temporal distribution model.

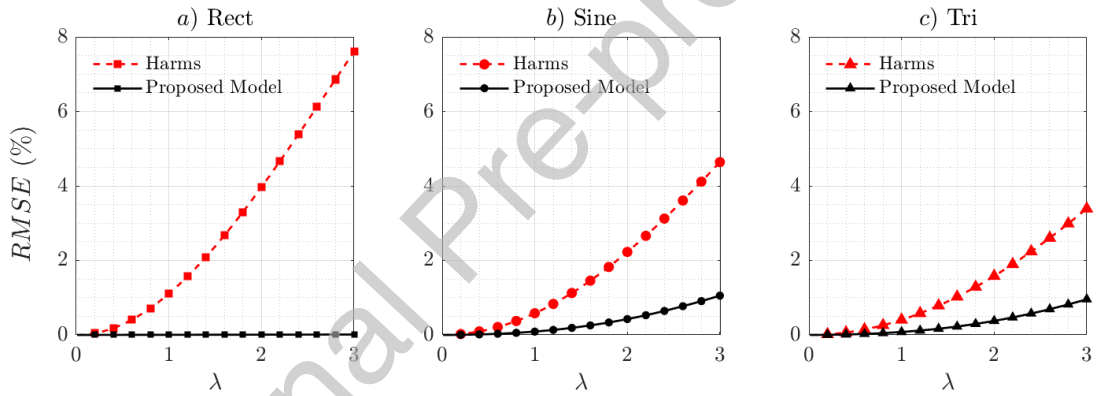

Fig.10. RMSE estimation of Harms's model and proposed model for *a)* Rect, *b)* Sine, and *c)* Tri functions.

3. EXPERIMENTAL SIGNAL ANALYSIS

The previous sections describe the progression in which the dynamic bias is defined and tested using simplified temporal signals. However, real life two-phase flows are complex due to their random turbulent behavior. The dynamic bias of experimental two-phase flow signals is analyzed in this section to give an idea of how the radiation transmission function deviates from its ideal behavior for various flow regimes. This is accomplished by converting high-temporal resolution wire-mesh sensor (WMS) signals along a hypothetical chord into a radiation transmission signal; this procedure was previously implemented by Manera [23] which showed proper agreement between the gamma densometer data and the converted WMS signal. It is important to clarify that WMS signals are used as the reference truth due to their high temporal resolution, on the other hand, actual radiation transmission measurements would have implicitly contained the dynamic bias that is being investigated.

The WMS measures the conductivity of the liquid and gas phases mapped over a plane. The temporal void fraction of the WMS data along the hypothetical chord direction is estimated as

$$\alpha(i,t) = \frac{1}{K}\sum_{k=1}^{K}\left(1 - \frac{u_{2\varphi}[i,k,t] - \bar{u}_G[i,k]}{\bar{u}_L[i,k] - \bar{u}_G[i,k]}\right), \quad \text{Eq.(41)}$$

where $\bar{u}_G$ is the average conductivity of the gas-phase , $\bar{u}_L$ is the average conductivity of the liquid-phase, $u_{2\varphi}$ is time dependent conductivity of the two-phase measurement, i and k are the spatially mapped voxels, and t is the measurement time. In the present study, we estimate the void fraction along the centerline where $i = CL$, and is averaged over the pixels along k. The temporal void fraction along the center line is then input into Eq.(12) to simulate radiation transmission measurement of the ideal function. The current study focuses on a 1-D arrangement for a point-source and point-detector system. Admittedly, advance radiation based systems such as computed tomography and radiography systems are spatially complex, these require expanding the modeling process of multiple individual detectors representative of these geometries, however this would be a topic for future investigations.

The present research deploys the WMS data belonging to the TOPFLOW facility benchmarked database obtained and reported by Lucas et al. [24, 25]; the representative flow regimes for this database are highlighted in Fig. 11. To briefly summarize, the TOPFLOW facility consists of a nominally 195.3 mm diameter and 8.0 m in length vertical steel pipe. The facility contains 6 injection layers which are logarithmically spaced away from the WMS plane located in the upper plenum of the facility, each injection layer is composed of 32 evenly distributed orifices characterized by a 4.0 mm diameter; the corresponding *L/D* relative injection distances away from the WMS are [1.4, 2.8, 7.7, 13, 22.9, 39.7]. The facility's operational (absolute) pressure is 0.25 MPa. The WMS is characterized by a 64x64 wire arrangement with a pitch of 3.0 mm between adjacent wires, and a gap distance of 2.0 mm between the transmission and the perpendicular-receptor layers. The WMS data acquisition was performed with a 2.5 kHz sampling frequency for a duration of 10 seconds. The data used in this study belongs to three flow regimes and one transitional flow; these are bubbly, bubbly to churn turbulent, churn turbulent, and wispy annular flow reported by Lucas. The selected datasets corresponds to those with a reported liquid superficial velocity of 1.017 m/s and with varying superficial gas velocity of [0.037, 0.14, 0.534, 2.038] m/s in respective order of ascending flow regimes; Table 1 summarizes the selected data sets used in the present study and these are highlighted in Fig. 11. The dynamic bias behavior for the hypothetical transmission system was estimated by using sampling periods divisible by the original experimental sampling period, this being 0.4 ms. The radiation transmission was simulated along the centerline of the pipe, therefore integrating the spatial void fraction data of the WMS along this chord-length. In this section, the dynamic bias will be normalized by the contrast attenuation factor λ, mindful that the maximum dynamic bias scales predominantly linearly in relation to $\lambda < 2$, nevertheless, at large values the behavior deviates from the linear growth. The contrast attenuation factor λ for this facility would correspond to a value of 1.71 for a ^{137}Cs isotopic-source, 1.91 for a ^{192}Ir isotopic-source, and 4.07 for an x-ray source. The integration period required to reach 90% of the asymptotic dynamic bias buildup value will also be reported for each flow regime in order to give perspective of the corresponding dynamic bias build time.

Table 1. WMS data sets matrix obtained from Lucas et al. [12].

Case	Identifier	Regime	J_L	J_G	Sampling

			[m/s]	[m/s]	Frequency [kHz]
1	074	Bubbly	1.017	0.037	2.5
2	107	Bubbly to Churn Turbulent	1.017	0.14	2.5
3	140	Churn Turbulent	1.017	0.534	2.5
4	173	Wispy Annular	1.017	2.038	2.5

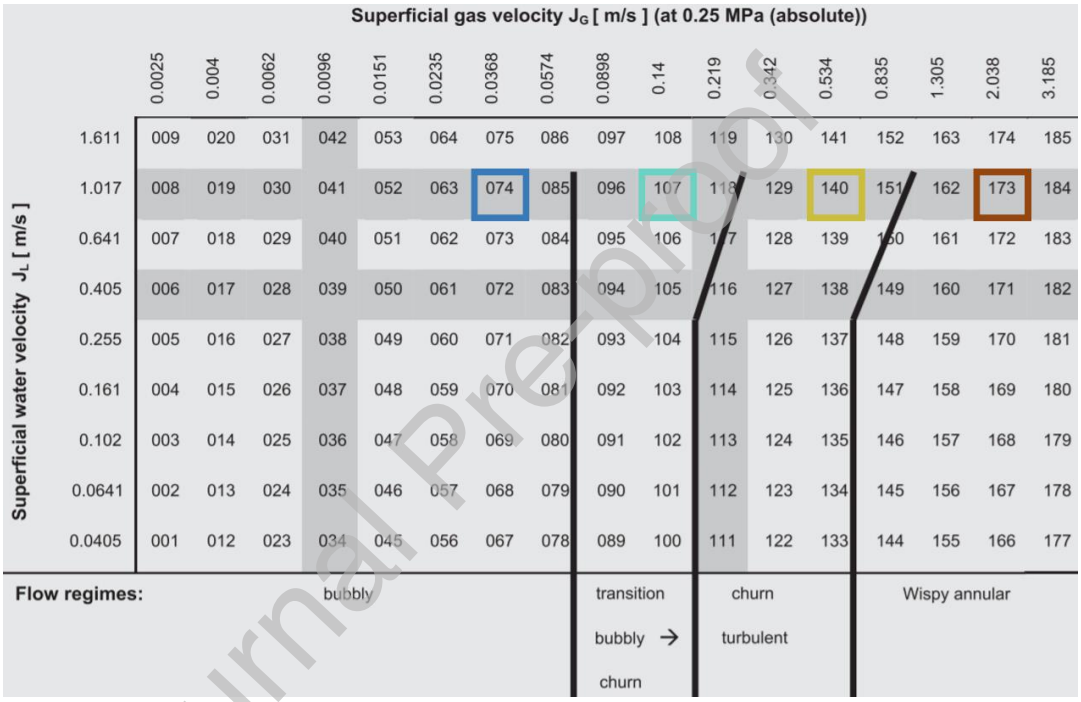

Fig. 11. TOPFLOW database obtained from and reported by Lucas et al. [24, 25]; highlighted are the selected datasets for ▫bubbly, ▫bubbly to churn turbulent, ▫ churn turbulent, and ▫ wispy annular.

4.1 Bubbly Flow

The first regime of interest is the bubbly flow, with a low superficial gas velocity of 0.037 m/s and a relatively low average void fraction. The parameters of interest are tabulate in Table 2, and are shown in Fig.12; the time-average spatial void fraction with the black plane representing the transmission centerline are shown in plot *a*, the centerline temporal void fraction is plotted in *b*, and the dynamic bias build up curves is plotted in *c* for the various L/D. The spatial void fraction visualizes how the gas is injected and remains near the wall with a slow cross migration towards the center of the pipe; full migration is accomplished at the last measurement length L/D = 39.7. The temporal void fraction signals are characteristically noisy due to the bubble size and quantity, best depicted by the temporal centerline void fraction. The standard deviation has a gradual increase in relation to the injection length with a max value

of 3.67% at L/D equal to 39.7. The normalized dynamic bias has a slight increase from the nearest to the furthest measurement length, however it is too small to attribute it to any effect. The values of $\Delta\alpha/\lambda$ are consistently small, below 0.1%, which can be considered negligible. The dynamic bias buildup period ranges from 58 ms to 141 ms at most from the obtained results, these correspond to sampling frequencies of 17.24 Hz and 7.08 Hz respectively; The results show that the buildup of the bias is relatively fast, however it becomes slower at the injection lengths L/D of 7.7 and 13; this is perhaps aided as the gas migrates towards the center of the pipe and the flow evolves.

Table 2. Bubbly Flow

Parameters	*L/D*	**1.4**	**2.8**	**7.7**	**13**	**22.9**	**39.7**
Centerline Avg. Flow	**Avg. Void Fraction** $\bar{\alpha}_{CL}$ [%]	2.29	1.90	2.26	2.82	4.47	6.57
	STD. $\sigma_{\alpha,CL}$ [%]	3.04	2.90	3.07	3.15	3.59	3.67
Dynamic Bias	**Norm. Asymptotic** $\Delta\alpha/\lambda$ [%]	0.04	0.04	0.05	0.04	0.06	0.07
	90% Buildup Int. Period T [ms]	58	82	135.2	141.2	76	88
	Equivalent Sampling Freq. f [Hz]	17.24	12.2	7.4	7.08	13.16	11.36

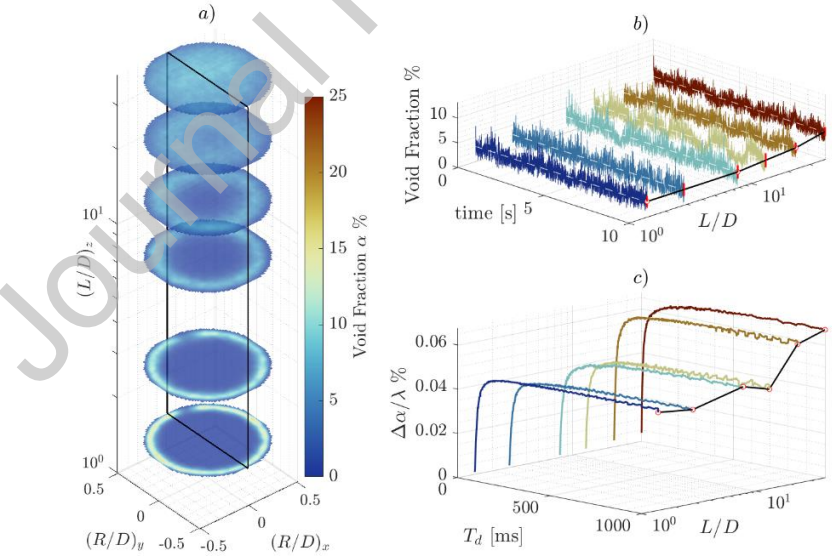

Fig.12. Analysis of bubbly flow regime: *a)* time-average spatial void fraction, *b)* temporal centerline void fraction, and *c)* dynamic bias build-up curves.

4.2 Bubbly to Turbulent Churn Flow

The transitional regime from bubbly to turbulent churn has a gas superficial velocity of 0.14 m/s; the flow analysis is shown in Fig.13 and reported in Table 3. The flow spatial progression shows a faster void fraction cross migration towards the center of the pipe, with a fully transitioned parabolic profile at L/D equal to 22.9. The centerline average void fraction shows an overall increase from 10.15% to 23.10%. The standard deviation increases from 5.06% for the nearest injection length to 7.89% for the furthest injection length, with the largest value located at L/D equal to 22.9. This effective increase in the standard deviation occurs as the sharp peaks depicted by the temporal centerline void fraction become more prominent at increased L/D. The normalized dynamic bias $\Delta\alpha/\lambda$ increases from 0.13% for the nearest length to 0.31% for the furthest length. The buildup integration period ranges from 88 ms to 221 ms, which correspond to sampling frequencies of 11.36 Hz to 4.52 Hz respectively. The results show that the buildup is the fastest at the smallest L/D, and the buildup of this error tends to get slower with increase in development length.

Table 3. Bubbly to Churn Turbulent

Parameters \ *L/D*		**1.4**	**2.8**	**7.7**	**13**	**22.9**	**39.7**
Centerline Avg. Flow	**Avg. Void Fraction** $\bar{\alpha}_{CL}$ [%]	10.05	12.90	17.79	17.56	20.74	23.10
	STD. $\sigma_{\alpha,CL}$ [%]	5.06	5.49	6.51	7.24	8.05	7.89
Dynamic Bias	**Norm. Asymptotic** $\Delta\alpha/\lambda$ [%]	0.13	0.15	0.21	0.27	0.34	0.31
	90% Buildup Int. Period T [ms]	88	178.8	159.2	182.8	187.2	221.2
	Equivalent Sampling Freq. f [Hz]	11.36	5.59	6.28	5.47	5.34	4.52

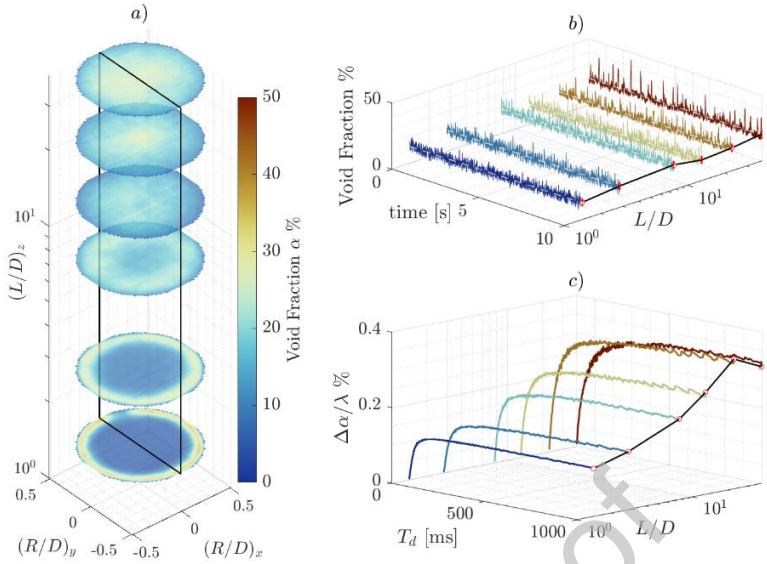

Fig.13. Analysis of transition from bubbly to turbulent churn regime: *a)* time-average spatial void fraction, *b)* temporal centerline void fraction, and *c)* dynamic bias buildup curves.

4.3 Turbulent Churn Flow

The second regime of interest is the fully transitioned turbulent churn flow with a gas superficial velocity of 0.534 m/s; the analysis is shown in Fig.14 and tabulated in Table 4. The time-average spatial void fraction shown in *a*) depicts how the gas phase has an increased cross migration at L/D of 7.7. The centerline void fraction steadily increases from 12.38% from the nearest length to 44.56% at the furthest length along the centerline, the standard deviation increases from 6.06% to 11.02% respectively representing a surge in fluctuations with increased distance, best depicted by the temporal centerline signal shown in Fig.14*b*. The value of $\Delta\alpha/\lambda$ increases from 0.19% for the nearest length to 0.61% for the furthest length, with its maximum value of 0.71% located at an L/D of 22.9. The dynamic bias buildup integration period ranges from 95 ms to 196 ms, corresponding to sampling frequencies of 10.5 Hz and 5.1 Hz. The buildup is faster near the closest injection length, and tends to get slower with increased injection length distance L/D.

Table 4. Churn Turbulent

Parameters \ L/D		1.4	2.8	7.7	13	22.9	39.7
Centerline Avg. Flow	**Avg. Void Fraction** $\bar{\alpha}_{CL}$ [%]	12.38	16.94	33.94	38.74	41.46	44.56
	STD. $\sigma_{\alpha,CL}$ [%]	6.06	9.22	11.20	11.27	11.77	11.02
Dynamic Bias	**Norm. Asymptotic** $\Delta\alpha/\lambda$ [%]	0.19	0.43	0.65	0.65	0.71	0.61
	90% Buildup Int. Period T [ms]	95.2	155.2	158	156	176	196

Equivalent Sampling Freq. f [Hz]	10.5	6.44	6.33	6.41	5.68	5.1

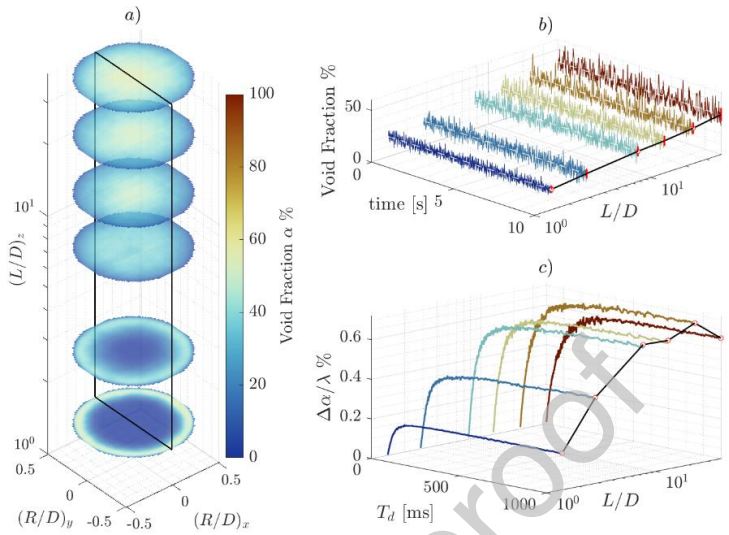

Fig.14. Analysis of turbulent churn regime: *a)* time-average spatial void fraction, *b)* temporal centerline void fraction, and *c)* dynamic bias buildup curves.

4.4 Wispy Annular Flow

The last regime investigated was the wispy annular flow with a gas superficial velocity of 2.038 m/s; the results are presented in Fig.15 and tabulated in Table 5. The spatial void fraction shown in *a*) further demonstrate how the gas phase promptly migrates towards the center of the pipe at L/D equal to 7.7. The centerline average void fraction increases from 39.89% at the nearest length to 70.32% at the furthest length, and the standard deviation ranges from 6.70% to 8.24%. The normalized dynamic bias $\Delta\alpha/\lambda$ varies across the measurement lengths from 0.22% at the nearest length to 0.32% at the furthest length, with the largest value of 0.34% at L/D equal to 2.8. The buildup integration period is 145.2 ms for the nearest length and 235.2 ms for the furthest length, corresponding to sampling frequencies 6.9 Hz and 4.25 Hz respectively. Similar to the previous flow regimes, the buildup is the fastest at the nearest injection length and tends to become slower with increase in injection length. This flow regime has overall the slowest buildup in comparison to the other flow regimes.

Table 5. Wispy Annular Flow

Parameters \ *L/D*		**1.4**	**2.8**	**7.7**	**13**	**22.9**	**39.7**
Centerline Avg. Flow	**Avg. Void Fraction** $\bar{\alpha}_{CL}$ [%]	39.89	46.04	65.22	66.65	68.95	70.32
	STD. $\sigma_{\alpha,CL}$ [%]	6.70	8.26	7.62	7.81	7.55	8.24
Dynamic Bias	**Norm. Asymptotic** $\Delta\alpha/\lambda$ [%]	0.22	0.34	0.28	0.29	0.28	0.32

90% Buildup Int. Period T [ms]	145.2	234	156	238	227.2	235.2
Equivalent Sampling Freq. f [Hz]	6.89	4.27	6.41	4.2	4.4	4.25

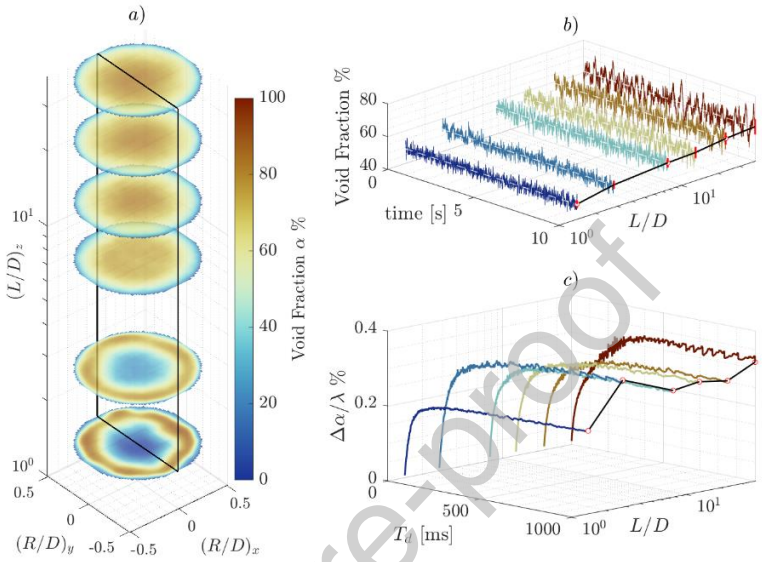

Fig.15. Analysis of wispy annular flow regime: *a)* time-average spatial void fraction, *b)* temporal centerline void fraction, and *c)* dynamic bias buildup curves.

4.5 Signal Characteristics

To develop a more accurate dynamic bias expression, a method was formulated in section 3.3 to simplify complex signals into a two-component rectangular signal model which preserves the original signal's average void fraction and variance. As reminder to the reader the active and passive amplitudinal displacement are denoted as ε^+ and ε^- respectively. The temporal distribution ω describes the fraction of time in which the signal is active, while $(1-\omega)$ dictates the fraction of time the signal is in the passive phase. In this section we further analyze the results obtained for the WMS data across different flow regimes.

The relation between the signal variance and the average void fraction is shown in Fig.16*a*. Here the general trend shows an increase in variance with increase in average void fraction for the regimes ranging from bubby to churn turbulent flow, however, the variance does not significantly change for the wispy annular regime. Fig.16*b* compares the active and passive amplitudinal components, in which the identity line represents equidistant or symmetric conditions between these components. The bubbly and bubbly to churn turbulent flows are characterized by their prominent active amplitudinal component, the churn turbulent flow falls closer to the identity line yet favors the active component, while the wispy annular regime lies around the identity line and is observed to have slightly more prominent passive components. Fig.16*c* depicts the temporal portion of the active component and compares it to the void fraction. The clusters representing the different regimes show that the temporal distribution does not significantly change, except in the case of the bubbly flow regime which does show an overall increase in active phase

duration. Overall, the regime progression shows a tendency to approach a symmetric temporal and amplitudinal distribution. Lastly, Fig.16*d* compares the areas underneath the active phase and passive phase; the addition of these areas represents the average void fraction, therefore it quantifies which phase has the most significant contribution. As it would be expected, the active phase is consistently the primary void fraction source; nevertheless, the data for bubbly to churn turbulent regimes also shows that there is equitable contributions between the active and passive phases for this regime.

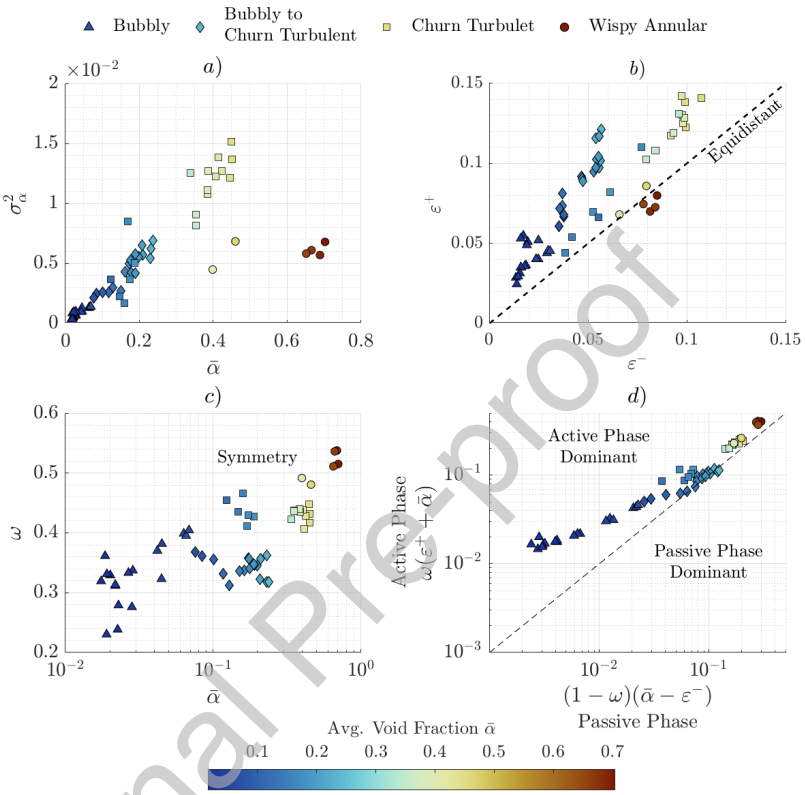

Fig.16. Experimental signal characteristics and components derived from the temporal distribution model. *a)* variance vs average void fraction, *b)* active and passive amplitudinal displacements, *c)* temporal distribution vs average void fraction, and *d)* equivalent active vs passive void fraction areas.

The objective of this discussion is to add another layer of understanding to the phenomena being investigated. Generally, the standard deviation of the signal quantifies the spread of the data away from the mean and whose bounds are typically assumed to be symmetric. However, there are instances where these fall out of range and do not fully capture the characteristics of the signal. Here we introduce additional components which enhance in a simple manner the analysis of these complex signals.

4.6 Dynamic Bias Results

The relation between the dynamic bias and the centerline variance for the investigated flow regimes are shown in Fig.17 for a $\lambda = 1$; the regimes are identified by individual markers and the color represents the average void fraction of the centerline signal. The dynamic bias strongly follows a linear scaling in relation to the signal's variance, the magnitude of all the signals analyzed remains below 1% for $\lambda = 1$; however, considering the turbulent churn regime and based on the scaling of the TOPFLOW paired with a

^{137}Cs isotopic-source can result in a void fraction error of ~1.3% and an x-ray source can result in a ~3.3% error.

The analysis comparing the ideal dynamic bias to Harms's model, and the proposed temporal distribution model are shown for each flow regime in Fig.18; Harms's model is shown as the red scatter dots, while the proposed model is shown in the black scatter dots, these are plotted along with the bias identity line. The results show that both models lie near the identity line, the proposed model falls closer to the identity line, this is most noticeable in the bubbly to churn turbulent and churn turbulent regimes; this is further shown in zoomed plots of the bubbly regime shown in Fig.18*a*. Analogous to the analysis performed in section 3.3, the RMSE was also estimated to compare the models prediction as a function of contrast attenuation factor λ for the studied flow regimes, the results are presented in Fig.19. The RMSE grows exponentially with λ, nevertheless it is considerably small throughout the flow regimes analyzed. However, comparing Harms's model and the proposed model shows that the latter has higher accuracy given that its RMSE magnitude is consistently below Harms's model for all cases. the RMSE percentage decrease for the proposed model relative to Harm's for the range of λ improves by 50% to 58% for the bubbly regime, 40% to 59% for the bubbly to churn transitional regime, 36% to 56% for the churn regime, and 15% to 56% for the wispy annular. This affirms that approximating the temporal distribution of the flow improves the estimation of the dynamic bias.

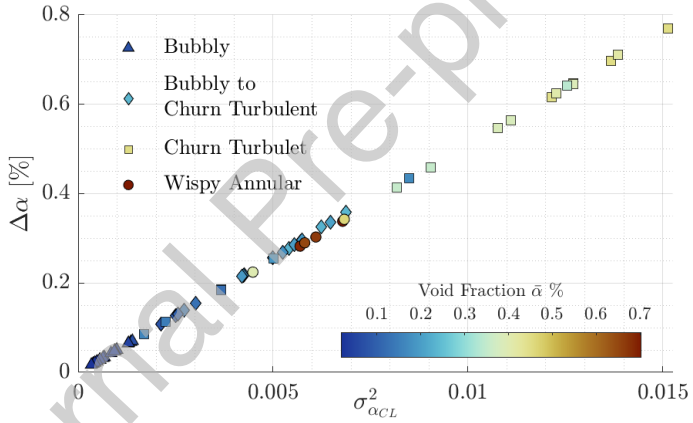

Fig.17. Dynamic bias relation to the experimental signal variance for λ=1.

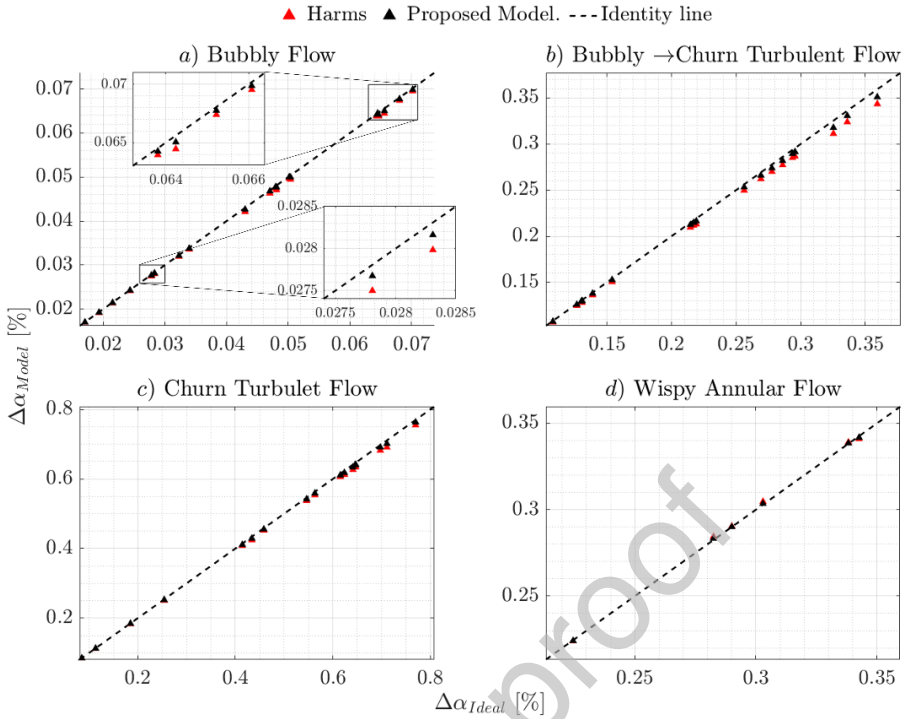

Fig.18. One to one comparison between the ideal dynamic bias, Harms's model, and the proposed model for *a)* bubbly flow, *b)* bubbly to churn turbulent flow, *c)* churn turbulent flow, and *d)* wispy annular flow.

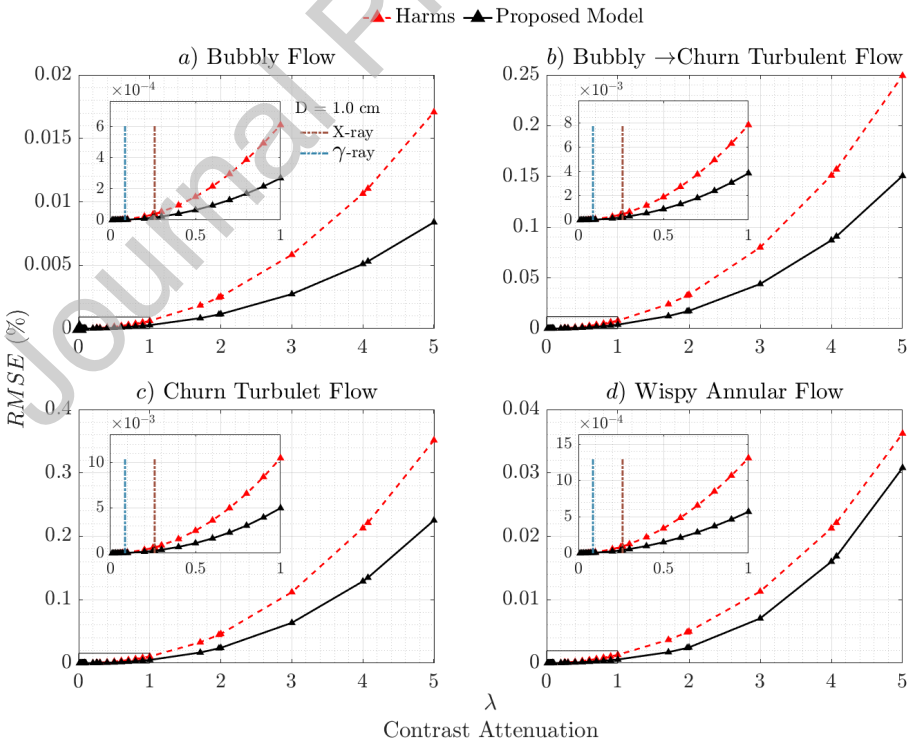

Fig.19. RMSE estimation of Harms's model and proposed model for *a)* bubbly flow, *b)* bubbly to churn turbulent flow, *c)* churn turbulent flow, and *d)* wispy annular flow.

4. CONCLUSIONS

The present study demonstrates that the dynamic bias in void-fraction measurements carried out using radiation transmission techniques is caused by an error buildup that occurs in the temporal integration of a time-varying exponential transmission function intrinsic to radiation detection measurements. A new analytical expression describing the dynamic bias was derived based on rectangular pulses. This new definition considers the effects that the temporal distribution ω, the amplitudinal distribution ξ, and the attenuation contrast factor λ have on the dynamic bias; the latter is a dimensionless parameter that is determined by the radiation trace-length through the flow region, as well as the liquid and gas linear attenuation coefficient which is dependent on the elemental composition of the working fluids, the type of radiation and its energy. The dynamic bias expression previously derived by Harms et al. [16] only focused on the amplitudinal component and assumed temporal symmetry, this expression is also encompassed in the new analytical definition. The rectangular pulse model serves as the ideal function to characterize the behavior, evolution, and the outermost limits of the dynamic bias. In addition, an expression for the critical temporal distribution which yields the largest dynamic bias was derived; this expression can be helpful in determining an experimental setup's susceptibility to the dynamic bias.

Next, numerical modeling following radiation transmission of simple void fraction signals was used to validate the methodology; the signals used include rectangular, sinusoidal, and triangular shaped pulses which were manipulated by modifying the duty cycle or full width half max such that it yields the predetermined average void fraction. The dynamic bias was then estimated from the simulated transmission signals, the detector integration window was varied in relation to the signal period. This showed that the dynamic bias builds up whenever the detector integration period is smaller than the phenomena period, and it reaches an asymptotic value when the detector period becomes equal or larger than the phenomena period. The buildup is shown to be reduced at fast sampling rates, given that under these conditions the flow appears to be moving slowly in respect to the detector measurement period. The asymptotic values of the dynamic bias obtained using 50% void fraction applied to the rectangular and sinusoidal signals matched to those reported by Andersson et al. [17] which validates the numerical modeling performed in this study. Additionally, the results obtained from the rectangular pulsed signals match the analytical results previously derived.

A method was developed to simplify arbitrary signals into an equivalent rectangular two-component model which preserves the average void fraction and the original signal's variance; the two-components refer to an active phase and a passive phase. The goal was to approximate the temporal distribution of the signal and from this, estimate the dynamic bias from the previously derived analytical expression. The dynamic bias prediction was compared for the three simplified signals between Harms's model and the proposed model. The results showed improvement in the dynamic bias prediction by the proposed model, which reinforces the importance of including the effects that the temporal distribution has on the dynamic bias.

In addition, experimental signals for bubbly, churn turbulent, and wispy annular flow regimes obtained from the TOPFLOW facility [24] using WMS sensors were used to simulate radiation transmission measurements of said flow regimes, and the associated dynamic bias was analyzed. The dynamic bias was less than 1% at a contrast attenuation factor of $\lambda = 1$ for the experimental flow regimes analyzed; the churn turbulent flow regime had the largest bias due to its inherently larger signal fluctuation. The values of TOPFLOW facility's contrast attenuation factor λ are 1.71 for a ^{137}Cs isotopic-source, and 4.07 for an

x-ray source; this can result in a bias magnitude of ~1.3% for a ^{137}Cs and ~3.3% for an x-ray source. Harms's and the proposed models were used to predict the dynamic bias of the experimental signals; the results found both models to have adequate performance, with the proposed model consistently presenting more accurate results. The 90% bias buildup period for the bubbly regime ranged from 58 ms to 141 ms, for the bubbly to churn turbulent transition was 88 ms to 221 ms, for the churn turbulent regime it was 95 ms to 196 ms, and for the wispy annular regime it was 145 ms to 238 ms; the fast buildup occurs at short injection lengths where the flow has not fully developed, this error tends to buildup slower at further injection distances in which the flow has been fully developed. It is also worth noting that the fast-range buildup becomes slower as the flow conditions transition from bubbly to wispy annular. Although the dynamic bias was not significant for the experimental signals analyzed, it is recognized that transient plug flows with large variance can increase the influence of the dynamic bias.

In order to minimize the undesired effects of this error, it is recommended to perform high-speed measurements while striking a balance in terms of radiation counts per frame for statistical certainty by choosing a detector system capable of fast acquisition paired with a strong radiation source to obtain adequate radiation statistics. From the flow condition aspect, this error will build up slower at low flow rate conditions, and will worsen with increase in flow rate, in addition to the development state of the flow as previously mentioned. Additionally, the size of the flow region should be carefully designed in consideration of the liquid and gas phase elemental composition to maintain a moderate contrast attenuation factor to distinguish the two phases while maintaining a small dynamic bias. External experimental materials (i.e., such as insulator, experiment housing, etc.) do not contribute to the dynamic bias, however, these reduce the available photon flux used for measurements, therefore it is suggested to use low-Z materials if possible or a strong source to avoid photon starvation. The presented study is representative of a single detector element, however, it lays the foundations for more complex radiation imaging systems comprised of several detector elements such as computed tomography and radiography systems. Concern is raised in the case of computed tomography measurements in which this error becomes embedded into the void fraction reconstruction through the algorithms implemented to perform imaging reconstruction; the effects from this should be subject of further investigation. Pairing of secondary measurement instrumentation such as WMS and needle probes can assist in determining the flow variance and temporal distribution to help approximate the dynamic bias magnitude intrinsic to the radiation transmission system and ultimately perform corrections if deemed significant.

The roles of the authors has been denominated as follows:

Julio Diaz: Conceptualization, Methodology, Software, Investigation, Data curation, Visualization, Formal Analysis, Writing- Original Draft

Juan Jose Serrano-Aguilera: Conceptualization, Investigation, Validation, Visualization, Writing- Reviewing & Editing.

Victor Petrov: Conceptualization, Data Curation, Resources, Investigation, Supervision, Funding acquisition, Project administration.

Annalisa Manera: Conceptualization, Supervision, Writing- Reviewing & Editing, Funding acquisition, Project administration

Declaration of interests

The authors declare that they have no known competing financial interests or personal relationships that could have appeared to influence the work reported in this paper.

ACKNOWLEDGEMENT

The authors of the present article are appreciative for the funding provided by the U.S. Nuclear Regulatory Commission through grant NRC-HQ-13-C-04-0022.

Appendix

A. Triangular Signal

The triangular pulsed signal can be described using piece wise temporal functions. The definition of ω represents the full width half max (FWHM) of the gas phase which in this case is equivalent to half of the pulse duration. In the present work, two separate definitions are used to generate the temporal void fraction functions, the first is used when the desired average void fraction is lower than ½. Here, the gas is pulsed with a maximum peak-to-peak amplitude ξ for the range $0 < \omega \leq 1/2$. Therefore, the liquid phase can be described as the remaining passive phase whenever the pulse is over. The signal can be defined by the piecewise relations as

$$\alpha_G(w,\xi) = \begin{cases} \dfrac{\xi w}{\omega} & \text{for } 0 \leq w \leq \omega \\ \xi\left(2 - \dfrac{w}{\omega}\right) & \text{for } \omega \leq w \leq 2\omega \\ 0 & \text{otherwise} \end{cases}. \qquad \text{Eq.(A.1)}$$

The variable w is used to sift through the signal cycle and the subscript G denotes the gas pulse. The average of the signal is obtained from the piecewise sections and can be expressed as

$$\bar{\alpha}_G(\omega,\xi) = \int_0^{\omega} \frac{\xi w}{\omega}\, dw + \int_{\omega}^{2\omega} \xi\left(2 - \frac{w}{\omega}\right) dw \qquad \text{Eq.(A.2.}a\text{)}$$

$$\bar{\alpha}_G(\omega,\xi) = \xi\omega. \qquad \text{Eq.(A.2.}b\text{)}$$

The variance of the gas pulse can then be defined as

$$\sigma^2_{\alpha_G} = \int_0^{\omega} \left(\frac{\xi w}{\omega} - \bar{\alpha}_G\right)^2 dw + \int_{\omega}^{2\omega} \left(\xi\left[2 - \frac{w}{\omega}\right] - \bar{\alpha}_G\right)^2 dw \qquad \text{Eq.(A.3.}a\text{)}$$

$$\sigma^2_{\alpha_G} = \frac{2\xi^2\omega}{3} - \xi^2\omega^2 \qquad \text{Eq.(A.3.}b\text{)}$$

The second definition of the triangular signal occurs in the case where the liquid phase is pulsed, and the gas phase is dominant. To remain congruent, the FWHM of the liquid pulse is defined as $(1-\omega)$, therefore the gas phase FWHM is defined $1/2 < \omega \leq 1$; the temporal void fraction in this case is defined as:

$$\alpha_L(w,\omega,\xi)=\begin{cases}1-\dfrac{w\xi}{1-\omega} & \text{for } 0\le w\le(1-\omega)\\ \xi\left(\dfrac{w}{1-\omega}-1\right) & \text{for } (1-\omega)\le w\le 2(1-\omega)'\\ \xi & \text{otherwise}\end{cases} \quad \text{Eq.(A.4)}$$

where the subscript L denotes liquid pulsed phase. The average void fraction is obtained following the process expressed in Eq.(A.2.a), this case simplifies to:

$$\bar{\alpha}_L(\omega,\xi)=\int_0^{(1-\omega)}1-\frac{w\xi}{1-\omega}\,dw+\int_{(1-\omega)}^{2(1-\omega)}\xi\left[\frac{w}{1-\omega}-1\right]dw+\int_{2(1-\omega)}^{1}\xi\,dw \quad \text{Eq.(A.5.}a\text{)}$$

$$\bar{\alpha}_L(\omega,\xi)=\ 1-\omega-\xi+2\xi\omega \quad \text{Eq.(A.5.}b\text{)}$$

The associated variance of the liquid pulse is

$$\sigma^2_{\alpha_G}(\omega,\xi)=\int_0^{(1-\omega)}\left(1-\frac{w\xi}{1-\omega}-\bar{\alpha}_G\right)^2dw+\int_{(1-\omega)}^{2(1-\omega)}\left(\xi\left[\frac{w}{1-\omega}-1\right]-\bar{\alpha}_G\right)^2dw+\int_{2(1-\omega)}^{1}(\xi-\bar{\alpha}_G)^2dw, \quad \text{Eq.(A.6.}a\text{)}$$

$$\sigma^2_{\alpha_G}(\omega,\xi)=\xi-\frac{4}{3}\xi^2+\omega-5\xi\omega+\frac{16}{3}\xi^2\omega-\omega^2+4\xi\omega^2-4\xi^2\omega^2. \quad \text{Eq.(A.6.}b\text{)}$$

Putting it all together, the triangular pulse applied in this study is defined as

$$\alpha_{Tri}(w,\xi)=\begin{cases}\alpha_G(w,\omega,\xi) & \text{for } 0<\omega\le\dfrac{1}{2}\\ \alpha_L(w,\omega,\xi) & \text{for } \dfrac{1}{2}<\omega\le 1\end{cases} \quad \text{Eq.(A.7)}$$

B. Sinusoidal Signal

The sinusoidal pulse or signal can also be described using piece wise temporal functions. Similarly, to the case shown in Appendix A, the gas is pulsed with a peak-to-peak amplitude ξ for a duration twice the FWHM. The signal can be described by the piecewise relations as

$$\alpha_G(w)=\begin{cases}\dfrac{\xi}{2}\left[\cos\left(\pi\left[\dfrac{w}{\omega}+1\right]\right)+1\right] & \text{for } 0\le w\le 2\omega\\ 0 & \text{otherwise}\end{cases}. \quad \text{Eq.(B.1)}$$

The average void fraction is

$$\bar{\alpha}_G(\omega,\xi)=\int_0^{2\omega}\frac{\xi}{2}\left[\cos\left(\pi\left[\frac{w}{\omega}+1\right]\right)+1\right]dw, \quad \text{Eq.(B.2.}a\text{)}$$

$$\bar{\alpha}_G(\omega,\xi)=\ \omega\,\xi. \quad \text{Eq.(B.2.}b\text{)}$$

The variance of this gas pulse is

$$\sigma_{\alpha_G}^2(\omega,\xi) = \int_0^{2\omega} \left(\frac{\xi}{2}\left[\cos\left(\pi\left[\frac{w}{\omega}+1\right]\right)+1\right] - \bar{\alpha}_G\right)^2 dw + \int_{2\omega}^{1} \bar{\alpha}_G{}^2\, dw \qquad \text{Eq.(B.3.}a\text{)}$$

$$\sigma_{\alpha_G}^2(\omega,\xi) = \frac{3\xi^2\omega}{4} - \xi^2\omega^2 \qquad \text{Eq.(B.3.}b\text{)}$$

Similarly as before, the liquid pulse is described based on the FWHM duration of the gas phase, this being $(1-\omega)$ throughout the range of $1/2 < \omega < 1$; the piecewise function is then

$$\alpha_L(w) = \begin{cases} \dfrac{\xi}{2}\left[\cos\left(\dfrac{\pi w}{1-\omega}\right)+1\right] & \text{for } 0 \le w \le 2(1-\omega) \\ \xi & \text{otherwise} \end{cases}. \qquad \text{Eq.(B.4)}$$

The average void fraction is

$$\bar{\alpha}_L(\omega,\xi) = \int_0^{2(1-\omega)} \frac{\xi}{2}\left[\cos\left(\frac{\pi w}{1-\omega,}\right)+1\right] dw + \int_{2(1-\omega)}^{1} \xi\, dw, \qquad \text{Eq.(B.5.}a\text{)}$$

$$\bar{\alpha}_L(\omega,\xi) = \omega\,\xi. \qquad \text{Eq.(B.5.}b\text{)}$$

and the variance is defined as

$$\sigma_{\alpha_L}^2(\omega,\xi) = \int_0^{2(1-\omega)} \left(\frac{\xi}{2}\left[\cos\left(\frac{\pi w}{1-\omega,}\right)+1\right] - \bar{\alpha}_L\right)^2 dw + \int_{2(1-\omega)}^{1} (\xi - \bar{\alpha}_L)^2\, dw, \qquad \text{Eq.(B.6.}a\text{)}$$

$$\sigma_{\alpha_L}^2(\omega,\xi) = \xi^2\left[\frac{5\,\omega - 1}{4} - \omega^2\right] \qquad \text{Eq.(B.6.}a\text{)}$$

The piecewise sinusoidal function implemented in this study is

$$\alpha_{Sine}(w,\xi) = \begin{cases} \alpha_G(w,\omega,\xi) & \text{for } 0 < \omega \le \dfrac{1}{2} \\ \alpha_L(w,\omega,\xi) & \text{for } \dfrac{1}{2} < \omega \le 1 \end{cases}. \qquad \text{Eq.(B.7)}$$

REFERENCES

1. Kok, H. V., & Van der Hagen, T. H. J. J. (1999). Design of a simulated void-reactivity feedback in a boiling water reactor loop. *Nuclear Technology*, 128(1), 1-11.
2. Schlegel, J. P., Sawant, P., Paranjape, S., Ozar, B., Hibiki, T., & Ishii, M. (2009). Void fraction and flow regime in adiabatic upward two-phase flow in large diameter vertical pipes. *Nuclear Engineering and Design*, 239(12), 2864-2874.
3. Hooker, H. H., & Popper, G. F. (1958). A gamma-ray attenuation method for void fraction determinations in experimental boiling heat transfer test facilities (No. ANL-5766). Argonne National Lab., Lemont, Ill.
4. Petrick, M., & Swanson, B. S. (1958). Radiation Attenuation Method of Measuring Density of a Two-Phase Fluid. *Review of Scientific Instruments*, 29(12), 1079-1085.
5. Sha, W. T., & Bonilla, C. F. (1965). Out-of-pile steam-fraction determination by neutron-beam attenuation. *Nuclear Applications*, 1(1), 69-75.

6. Stahl, P., & von Rohr, P. R. (2004). On the accuracy of void fraction measurements by single-beam gamma-densitometry for gas–liquid two-phase flows in pipes. *Experimental Thermal and Fluid Science*, 28(6), 533-544.
7. Kumamaru, H., Kondo, M., Murata, H., & Kukita, Y. (1994). Void-fraction distribution under high-pressure boil-off conditions in rod bundle geometry. *Nuclear Engineering and Design*, 150(1), 95-105.
8. Breitenmoser, D., Manera, A., Prasser, H. M., & Petrov, V. (2019). High-resolution high-speed void fraction measurements in helical tubes using X-ray radiography. In 18th International Topical Meeting on Nuclear Reactor Thermal Hydraulics (NURETH-18) (pp. 3554-3567). American Nuclear Society.
9. Zboray, R., & Trtik, P. (2019). In-depth analysis of high-speed, cold neutron imaging of air-water two-phase flows. *Flow Measurement and Instrumentation*, 66, 182-189.
10. Morooka, S., Ishizuka, T., Iizuka, M., & Yoshimura, K. (1989). Experimental study on void fraction in a simulated BWR fuel assembly (evaluation of cross-sectional averaged void fraction). *Nuclear Engineering and Design*, 114(1), 91-98.
11. Bieberle, A., Hoppe, D., Schleicher, E., & Hampel, U. (2011). Void measurement using high-resolution gamma-ray computed tomography. *Nuclear Engineering and Design*, 241(6), 2086-2092.
12. Kataoka, I., Ishii, M., & Serizawa, A. (1984). Local formulation of interfacial area concentration and its measurements in two-phase flow (No. NUREG/CR--4029). Argonne National Lab.
13. Kataoka, I., Ishii, M., & Serizawa, A. (1994). Sensitivity analysis of bubble size and probe geometry on the measurements of interfacial area concentration in gas-liquid two-phase flow. *Nuclear Engineering and Design*, 146(1-3), 53-70.
14. Prasser, H. M., Böttger, A., & Zschau, J. (1998). A new electrode-mesh tomograph for gas–liquid flows. *Flow Measurement and Instrumentation*, 9(2), 111-119.
15. Harms, A. A., & Forrest, C. F. (1971). Dynamic effects in radiation diagnosis of fluctuating voids. *Nuclear Science and Engineering*, 46(3), 408-413.
16. Harms, A. A., & Laratta, F. A. R. (1973). The dynamic-bias in radiation interrogation of two-phase flow. *International Journal of Heat and Mass Transfer*, 16(7), 1459-1465.
17. Andersson, P., Sundén, E. A., Svärd, S. J., & Sjöstrand, H. (2012). Correction for dynamic bias error in transmission measurements of void fraction. *Review of Scientific Instruments*, 83(12), 125110.
18. Hampel, U., & Wagner, M. (2011). A method for correct averaging in transmission radiometry. *Measurement Science and Technology*, 22(11), 115701.
19. Hampel, U., Bieberle, A., Hoppe, D., Kronenberg, J., Schleicher, E., Sühnel, T., ... & Zippe, C. (2007). High resolution gamma ray tomography scanner for flow measurement and non-destructive testing applications. *Review of Scientific Instruments*, 78(10), 103704.
20. Wagner, M., Bieberle, A., Bieberle, M., & Hampel, U. (2017). Dynamic bias error correction in gamma-ray computed tomography. *Flow Measurement and Instrumentation*, 53, 141-146.
21. Carmignato, S., Dewulf, W., & Leach, R. (Eds.). (2018). Industrial X-ray computed tomography. Berlin: Springer International Publishing.
22. Knoll, G. F. (2010). Radiation detection and measurement. John Wiley & Sons.

23. Manera, A. (2003). Experimental and analytical investigations on flashing-induced instabilities in natural circulation two-phase systems: Applications to the startup of boiling water reactors, PhD Dissertation, Delft University of Technology, The Netherlands.

24. Lucas, D., Beyer, M., Kussin, J., & Schütz, P. (2010). Benchmark database on the evolution of two-phase flows in a vertical pipe. *Nuclear engineering and design*, 240(9), 2338-2346.

25. Lucas, D., Beyer, M., Szalinski, L., & Schütz, P. (2010). A new database on the evolution of air–water flows along a large vertical pipe. *International Journal of Thermal Sciences*, 49(4), 664-674.